LLNL-TH-443411

LAWRENCE
LIVERMORE
NATIONAL
LABORATORY

Thick Nano-Crystalline Diamond #films for fusion applications

C. Dawedeit

July 19, 2010

Disclaimer

This work performed under the auspices of the U.S. Department of Energy by Lawrence Livermore National Laboratory under Contract DE-AC52-07NA27344.

NTech
Lehrstuhl für
Nukleartechnik

Lawrence Livermore
National Laboratory

Technische Universität München

Diplomarbeit

by cand. Ing. Christoph Dawedeit
Registration Number: 2935778

Thick Nano-Crystalline Diamond films for fusion applications

Advisor TUM:	Prof. Dr. Rafael Macián-Juan
Advisor LLNL:	Dr. Jürgen Biener
Issued:	Monday, January 4, 2010
Submitted:	Wednesday, June 30, 2010

Eidesstattliche Erklärung

Hiermit versichere ich, die vorliegende Arbeit selbstständig und ohne Hilfe Dritter angefertigt zu haben. Gedanken und Zitate, die ich aus fremden Quellen direkt oder indirekt übernommen habe, sind als solche kenntlich gemacht. Diese Arbeit hat in gleicher oder ähnlicher Form noch keiner Prüfungsbehörde vorgelegen und wurde bisher nicht veröffentlicht.

Ich erkläre mich damit einverstanden, dass die Arbeit durch den Lehrstuhl fuer Nukleartechnik der Öffentlichkeit zugänglich gemacht werden kann.

Livermore Kalifornien, den 30. Juni 2010

Christoph Dawedeit

Abstract

This Diplomarbeit deals with the characterization of 9 differently grown diamond samples. Several techniques were used to determine the quality of these specimens for inertial confinement fusion targets. The quality of chemical vapor deposition diamond is usually considered in terms of the proportion of sp3-bonded carbon to sp2-bonded carbon in the sample. For fusion targets smoothness, Hydrogen content and density of the diamonds are further important characteristics. These characteristics are analyzed in this thesis.

The research for thesis was done at Lawrence Livermore National Laboratory in collaboration with the Fraunhofer Institut für angewandte Festkörperphysik Freiburg, Germany. Additionally the Lehrstuhl fuer Nukleartechnik at Technical University of Germany supported the work.

Contents

1 Introduction

The sun's energy source - nuclear fusion is viewed as a potentially important option to sustainably secure the energy demand of the future [23, 56, 49, 50, 28, 47]. The National Ignition Facility (NIF) will deliver up to 1.8 MJ laser light which will allow to prove the feasibility of inertial confinement fusion [45, 46]. The availability of robust fusion targets is an important requirement to achieve these goals. Targets are thin-walled, millimeter sized, spherical shells made out of a low atomic number material. A thin, frozen layer of deuterium tritium within these shells serves as fusion fuel [38, 37]. To start the fusion process the laser light is converted into soft x-rays to ablate the target. Due to this ablation the fuel is compressed to the density that is 50 times of gold which is about $1,000\frac{g}{cm^3}$ and exceeds 10^6 Kelvin. This compression drives the fuel to fuse together and form; helium, a neutron, and 17.6 MeV of energy.

One promising candidate as target material is high density carbon - diamond. The major advantage of diamond compared to other low atomic number materials is the high density which allows it to absorb more energy before it implodes. The more energy the target material absorbs the higher the efficiency of the fusion process. Further important requirements are; purity of the material, geometry of the target and surface roughnesses. The goal is to develop ultra-smooth thick Nano-Crystalline Diamond films for the inertial confinement fusion target application.

Nine different flat diamond samples with grain sizes between several microns to the Nano-Crystalline range are characterized in this thesis. During the growth process of the diamonds (in microwave plasma assisted chemical vapor deposition) two parameters were changed to influence the grain size: the Methane concentration and temperature. Additionally the effect of nanoseeding was examined. These specimen were systematically characterized for:

- surface morphology
    - Optical microscopy
    - Scanning Electron Microscopy
    - Atomic Force Microscopy
    - White Light Interferometry
- grain structure
    - X-Ray Diffraction
    - Raman Spectroscopy
    - Scanning Electron Microscopy

- chemical composition
    - Elastic Recoil Detection
    - Fourier Transform Infrared Spectroscopy
    - Near Edge X-Ray Absorption Fine Structure
    - Raman Spectroscopy
- mechanical properties
    - Density
    - Three point bending test

Followed by this introduction is a short paragraph which explains the two major approaches to achieve nuclear fusion. The next paragraph gives a brief overview about the Lawrence Livermore National Lab with a description of the National Ignition Facility and the target design. It ends with an overview of the Nanoscale Synthesis and Characterization Laboratory - the team I am working with. Afterwards the experimental techniques mentioned above are described in detail. The major chapter analyzes the diamonds. The end of the thesis summarizes the results and gives a perspective for the future.

2 Fusion Types

Basically there are magnetic confinement fusion and inertial confinement fusion to achieve controlled nuclear fusion to conduct energy research and perform high density physics (astrophysics) experiments. There are three critical values for nuclear fusion:

1. Time
2. Temperature
3. Pressure

The product of these three variables has to exceed a critical value to achieve fusion. The two approaches distinguish in a low pressure and long time process or high pressure and short time fusion.

2.1 Magnetic Confinement Fusion

Magnetic confinement fusion is a long time (several minutes) process for burning a heavy Hydrogen plasma. It is proposed to get a self sustaining plasma after igniting it once, to harvest energy from it. Fuel has to be added to keep the process alive and the fusion product Helium as well as other debris has to be extracted by the divertor. The plasma is confined by magnets at a low density. A magnetic field traps the plasma which is flying in a doughnut touching only specially designed parts, like the divertor. There are different approaches for the magnetic configurations. The most famous one is the Tokamak configuration. Heating for ignition comes from the magnetic field by ohmic resistance. Supplementary heating is provided by neutral beam injection and high frequency electromagnetic waves. Temperatures up to 150 million °C are achieved to ignite the fusion process [24].

ITER is the most promising experimental reactor which is currently build in Caderache France. It is supposed to start its first experiments in 2018. Further experiments should keep the plasma alive for about 1000 seconds [24].

2.2 Inertial Confinement Fusion

Inertial confinement fusion is an approach which confines small volumes by its inertia in a short time. A capsule with a diameter in the mm range is filled with thermonuclear fuel. To reach fusion the capsule surface is ablated driving the capsule to implode. This blow-off rapidly compresses the fuel to high densities. Due to this compression the fuel ignites and the fuel burns. The ablation of the capsule could be done with a laser or heavy ion beam approaches [69]. For a continuous energy yield several capsules per second have to be ignited.

Currently the National Ignition Facility focuses on this approach. First experiments with Deuterium Tritium fuels are scheduled for 2010-2011.

Summary Fusion Types

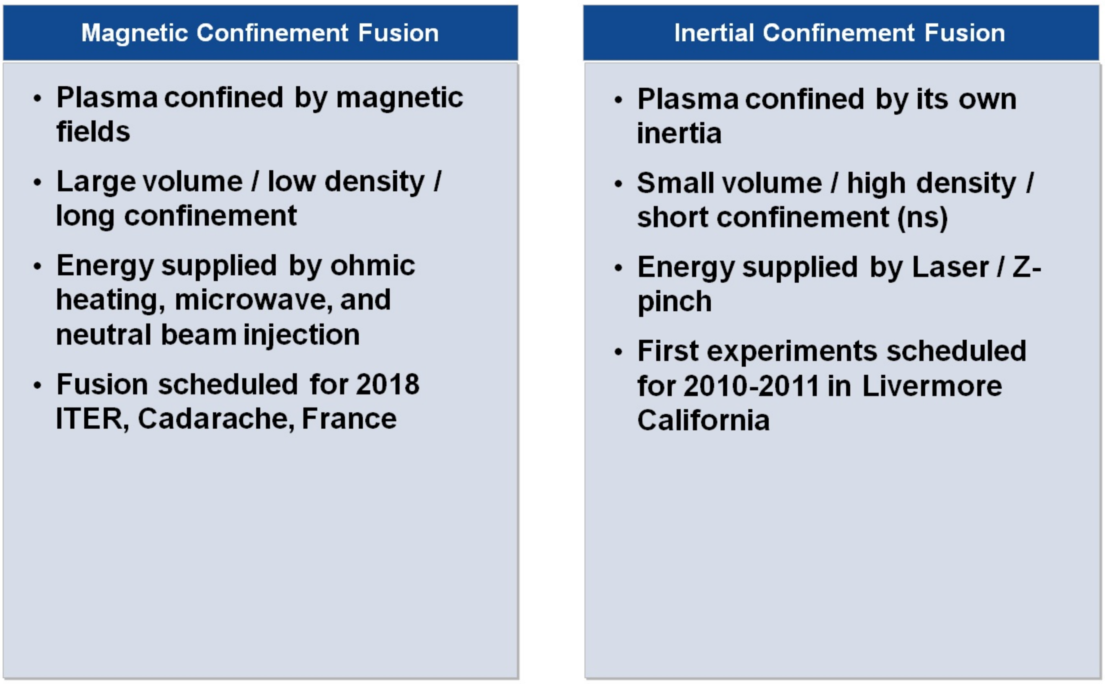

Magnetic Confinement Fusion

- Plasma confined by magnetic fields
- Large volume / low density / long confinement
- Energy supplied by ohmic heating, microwave, and neutral beam injection
- Fusion scheduled for 2018 ITER, Cadarache, France

Inertial Confinement Fusion

- Plasma confined by its own inertia
- Small volume / high density / short confinement (ns)
- Energy supplied by Laser / Z-pinch
- First experiments scheduled for 2010-2011 in Livermore California

Figure 2.1: Summary fusion types

3 Fusion at Lawrence Livermore National Laboratory

3.1 Lawrence Livermore National Laboratory

The Lawrence Livermore National Laboratory is a scientific research laboratory located in Livermore, California. It is primarily funded by the United States Department of Energy (DOE). Two of its main facilities are the Advanced Simulation and Computing Facility and the National Ignition Facility

The Laboratory was founded in 1952 as a nuclear research facility. The Laboratory was part of a plan to increase the national security during the Cold War. It was created as a competitor for the Los Alamos National Laboratory. E.O. Lawrence from the University of California Berkeley was searching for a site for large-scale science experiments.That is why the activities began in Livermore under the aegis of the University of California.

The 1970s were important for the current focus of Livermore. The energy crises forced the government of the United States to improve energy research. The goal was to develop a long-term reliable, affordable and clean source of energy. The first laser program was launched and Livermore still stands in the forefront of laser technology. Due to this knowledge and research the lab focuses on inertial confinement fusion. Currently the largest laser system worldwide is the National Ignition Facility located in Livermore.

The 2010s will probably be influenced by the National Ignition Facility combining strong fields of the laboratory: high density physics like astrophysics and energy research.

3.2 Nanoscale Synthesis and Characterization Laboratory

The Nanoscale Synthesis and Characterization Laboratory's (NSCL) primary mission is to create and advance interdisciplinary research and development opportunities in nanoscience and technology. Currently NSCL focuses on [21]:

1. Nanoporous materials, e.g. [74]
2. Ultrasmooth Nano-Crystalline Diamond for fusion applications, e.g. [3]
3. Filling of fusion capsules with aerogels
4. Material characterization, some characterization instruments are mentioned below.
5. Beryllium ablators

6. Deuterium Tritium ice layer formation
7. Material doping with atomic layer deposition
8. Nano-Crystalline materials

This Diplomarbeit is part of the ultrasmooth diamond development for fusion applications.

3.3 National Ignition Facility

The National Ignition Facility (NIF) is the most promising driver to prove the inertial confinement fusion approach. The physical construction of NIF started in May 1997. NIF consists of 192 lasers which focus on one point in the target chamber. It is the world's most powerful laser system. The construction was completed in March 2009. The lasers will produce 1.8 MJ laser energy in the ultraviolet. All this energy is concentrated onto a one centimeter scale fusion target to ignite a deuterium-tritium fuel capsule as described in chapter 2.2. This target attempts to reach temperatures of 100 million Kelvin and a density of $1000\frac{g}{cm^3}$. This entire process will take a few picoseconds [35] and will release energy in the order of 10 to 75 MJ [48].

NIF mainly consists of two laser bays and the target chamber (Figure 3.1a). The laser bays are about 300 m long and each is about 40 m wide. Between both of them there are the control center and various smaller devices. The target chamber is a ten meter diameter sphere with a high-vacuum. It is equipped with about 35 different diagnostics to study the target behavior. All 192 beam lines enter the target chamber. The target positioning system holds the target in the middle of the sphere (Figure 3.1b).

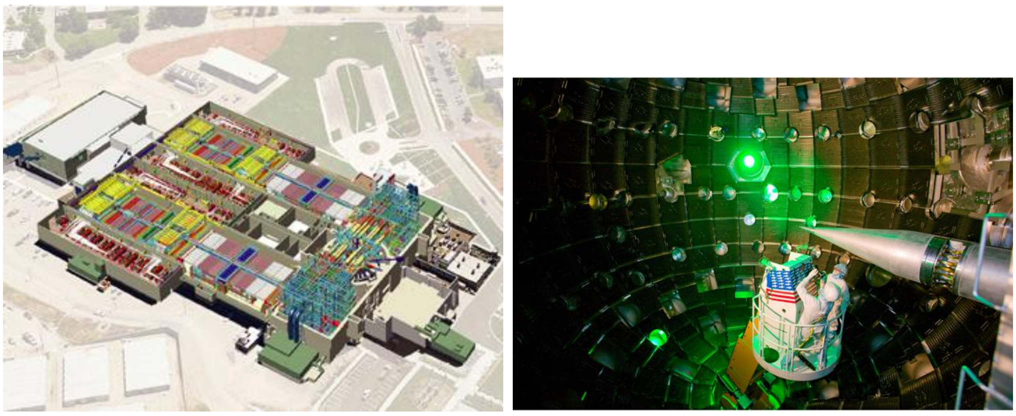

(a) (b)

Figure 3.1: 3.1a shows the National Ignition Facility. The lasers on the upper and lower part of the picture and the target chamber on the right side in the middle. 3.1b is the target chamber from the inside with the target positioning system coming from the right

The seed-laser-pulse starts really small produced by a cw Yb-doped-fibre. This device is responsible for the shape of the laser pulse, which has to be adjusted for different targets. Afterwards it is split to 48 equal laser pulses and send into preamplifier modules. Pulses from each of the 48 preamplifier modules are further split and delivered into the 192 beamlines (Figure 3.2). Each beam is expanded to a square of $37x37cm^2$ and amplified twice by power amplifiers and four times by the main amplifier. In this case it is a flashlamp-pumped Nd:glass laser operating at wavelengths of about $1053nm$ [51]. The Pockels cell changes the polarization of the laser once that the main amplifier can amplify four times. The deformable mirror mainly corrects wavefront distortions. After this entire process the laser passes through the switchyard which makes sure that all laser beams arrive at the same time at the target. Just before the beam enters the target chamber the wavelength is converted to $351nm$ and a focal lens concentrates the beam on the target [47].

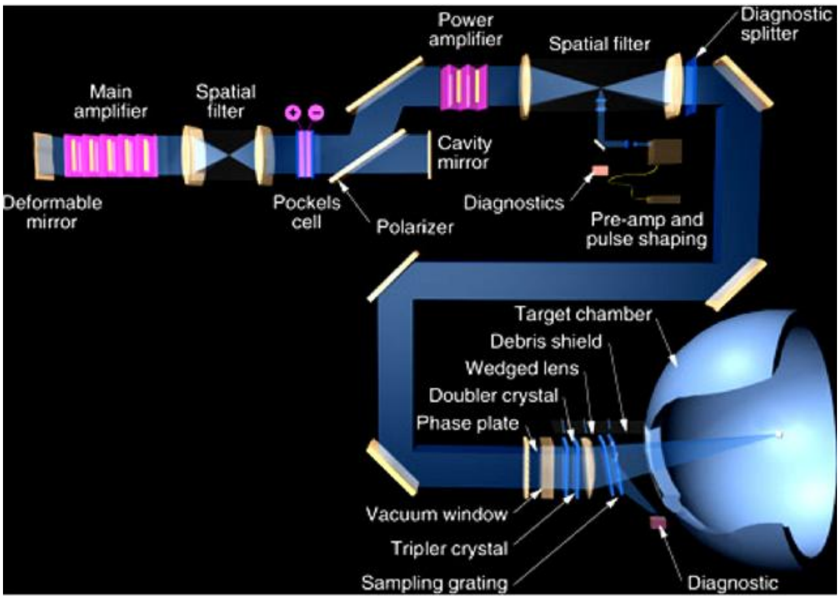

Figure 3.2: Describes one of NIF's 192 beamlines. The laser is amplified several times before entering the target chamber through various lenses

The National Ignition Facility has three missions. To strengthen basic nuclear research is one of them. Due to the high neutron flux the National Ignition Facility creates a unique environment in which to perform nuclear physic measurements. Studying high-energy-density science is another mission. Especially for basic science in astrophysics, planetary physics, hydrodynamics and material science these experiments are insightful. Since materials undergo fundamental changes at temperatures above $10000K$ and pressures above a gigabar the National Ignition Facility can pursue these research. The third mission is to prove fundamentals of nuclear fusion [47]. Fusion research results may help to build power plants which could supply the increasing energy demands and do not emit carbon [48].

NIF plans to achieves fusion by firing all 192 laser beams on a small tube called 'hohlraum' which contains the ablator shell. The target consisting mainly of the hohlraum and ablator shell, attached to a large sample positioner holding it in the middle of the target chamber. The hohlraum has about the length of 1 cm and the diameter of 0.5 mm. It is attached to the holder with two silicon arms which have the additional function to cool the hohlraum by conduction to about 18 K (figure 3.3a). Within this hohlraum there is the capsule with a frozen layer of deuterium tritium (figure 3.3b). This spherical capsule has a diameter of about 2 mm and could be made out of different materials like beryllium, CH (plastic) or high density carbon (diamond).

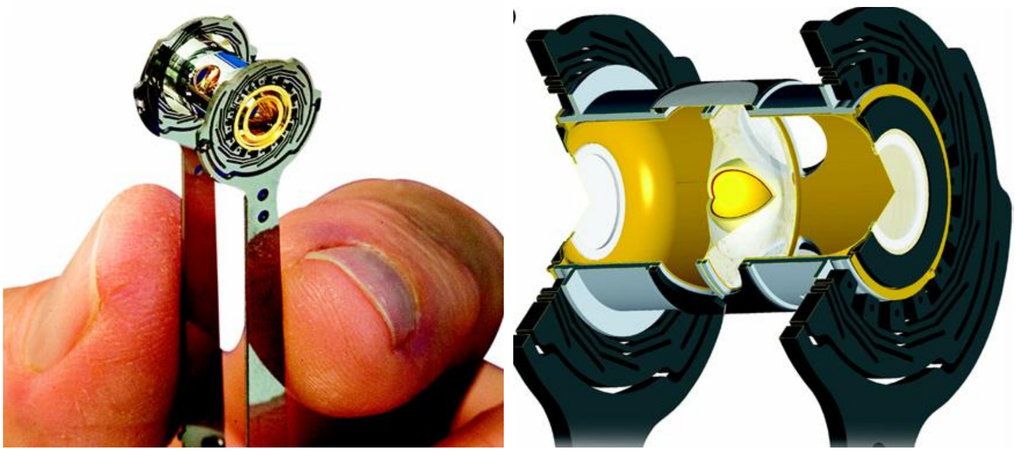

(a) (b)

Figure 3.3: 3.3a shows the dimension of a target relative to human fingers. Two silicon arms hold the target. 3.3b illustrates the ablator shell inside a hohlraum. The capsule diameter is about 2mm and the hohlraum length about 1cm.

Several concepts for imploding the capsule exist (figure 3.4a, 3.4b and 3.4c). NIF uses the indirect principle in which the laser beams hit the hohlraum first. The laserbeam with the wavelength of 351 nm will be absorbed by the interior wall and converted soft x-rays. Those x-rays bath the capsule and ablate its outer layer. Due to the ablation the capsule implodes, compresses the fuel and ignites the fuel. Since only a small part of the deuterium tritium in the middle of this imploded sphere gets hot enough to ignite its surrounding, it is called hot spot ignition [48]. For the laser light to x-ray conversation the hohlraum is built out of materials with a high atomic (Z) number. The advantage of this indirect drive is that small variations of the focus points can be tolerated, which makes the x-ray bath more homogeneous for the capsule. The hohlraum will be hit by an outer and inner cone of laser beams from each side. There are 32 beams for each inner cone and 64 for each outer cone, which are adjusted to make the entire x-ray field homogeneous. The direct drive would be more energy efficient but needs very accurate lasers. NIF can be configured to the direct drive arrangement in future. An alternative approach is the fast ignition concept that is comparable to a gasoline engine. First the fuel gets compressed by lasers and afterwards one powerful laser ignites it. This technique has the future potential to significantly increase the target gain or reduce the total energy required to achieve ignition [42].

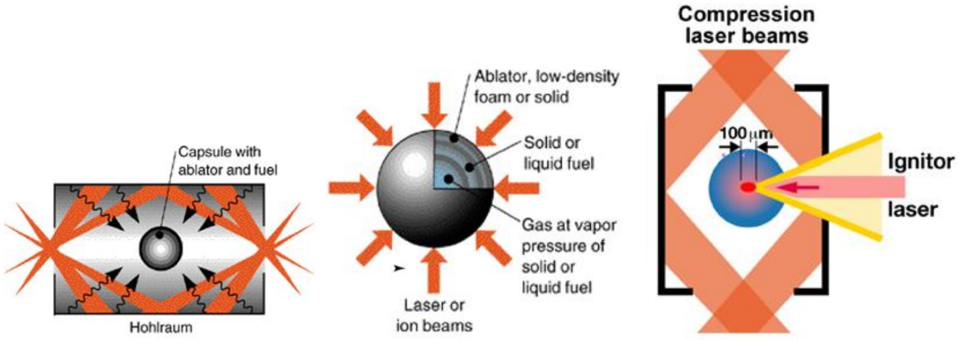

(a) (b) (c)

Figure 3.4: 3.4a describes the indirect drive approach for nuclear fusion. The lasers enter the hohlraum from the sides, reflect from the walls and homogeneously bath the ablator shell. In 3.4b lasers hit the fuel capsule directly, called direct drive. The approach in 3.4c is called fast ignition which is comparable to a gasoline engine. Laserbeams compress the ablator and another laser ignites the target.

The National Ignition Facilitysupports basic research and energy science. The major elements which this campaign has to achieve is to start ignition. The time frame to achieve this is 2006-2012. After completing this goal the National User Facility will be a platform for all research related to fusion. The National Ignition Campain is supported by many partners: General Atomic, Los Alamos National Lab, Sandia National Lab, National Nucler Security Admission, Laboratory for Laser Energetics, Atomic Weapons Establishment, Commissariat à l'énergie atomique and the Lawrence Livermore National Lab.

Designing the capsules as well as the hohlraums is a challenge on the nanometer scale. For example the laser entrance holes at the hohlraum must have a concentricity of $10\mu m$ to the hohlraum [20]. Capsules have many important requirements. First the shape has to be perfectly spherical with a required thickness uniformity of 10^{-4}. Second the roughness of both the outer and inner ablator shell surface has to be better than $10nm$ RMS. Third the fuel has to be uniformly condensed on the inner surface through a $5\mu m$ hole at 1.5°C below the triple point with an accuracy of $1mK$ [3, 47]. These and many more requirements make it a demanding task to develop capsules for inertial confinement fusion.

3.4 Diamond as ablator shell

Diamonds have many outstanding material properties which make them interesting for many industries. Possible applications are antiwear coatings, optical windows, fusion targets and electrochemical electrodes which translates in the following physical properties: high hardness, chemical inert, high thermal conductivity, high atomic density, high yield strength and thermal stability [4, 3, 31, 72]. For producing artificial diamonds chemical vapor deposition (CVD) or High Pressure High Temperature synthesis is used. High Pressure High Temperature is generally used to produce bulk diamond like nano diamond particles – CVD to grow thin layers like coatings. In a CVD process the diamond is deposited on a carrier medium which usually is silicon wafer. The growing process starts with dispersed diamond particles on the silicon wafer in a several hundred degree atmosphere. This atmosphere consists of Methane and Hydrogen. By activating this plasma with a hot fillament or microwave $CH_3\bullet$ radicals and atomic Hydrogen is produced. $C_2H_3\bullet$ is responsible for the growth of the diamond and the atomic Hydrogen etches non-diamond phases [11]. Etching is necessary due to the thermodynamical instability of diamond which always co-deposits graphite and amorphous carbon. The diamonds analyzed in this thesis were grown with a microwave plasma assisted CVD. Figure 3.5 shows the diamond surrounded by hot CH_4 and H_2 gas. A special ellipsoidal geometry heats the microwave plasma only above the sample. Diamonds grown with this approach are more pure than those diamonds contaminated by hot filament chemical vapor deposition. The Fraunhofer Insitut in Freiburg, Germany produced the diamond films characterized in this thesis.

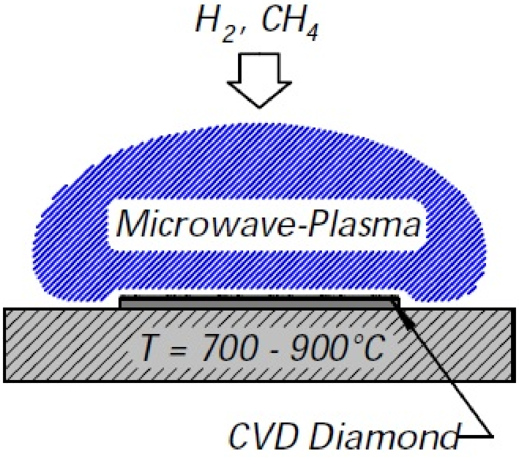

Figure 3.5: This figure describes microwave plasma assisted chemical vapor deposition. The heat through the microwave activates the plasma to atomic Hydrogen and $CH_3\bullet$ radicals. The latter is responsible for the diamond growth on a silicon waver and the atomic Hydrogen etches non-diamond phases.

Several papers already describe the properties of Nano-Crystalline Diamonds [71, 8, 73, 33, 31]. The goal of this thesis is to develop ultra-smooth thick Nano-Crystalline Diamond films grown by microwave assisted CVD for the inertial confinement fusion application. These results are of particular interest for High Energy Density physics which are necessary to understand the ablation process for fusion targets. It is important to ensure that the ablator does not spend time in a partially melted state in which velocity variations could seed Rayleigh-Taylor instabilities [3]. An important factor is the density of the material which is needed as an input to analyze High Energy Density Physics experiments. Additionally the Hydrogen content, the sp^2 carbon concentration, grain size and the surface roughness are important for High Density Physics and NIF experiments. This thesis analyzes these parameters.

3.5 Definition of different artificial Diamonds

Diamonds are defined by grain size [31, 70]:

1. Single-Crystalline Diamond: Diamonds just consisting out of one grain.
2. Micro-Crystalline Diamond: Grain size $> 0.1\mu m$ but not single crystalline
3. Nano-Crystalline Diamond. Grain size 50nm - 100nm
4. Ultra-Nano-Crystalline Diamond: Grain Size $< 50nm$

There are no exact borders for the different kinds of diamonds. Samples characterized in this thesis range from several micron crystalline to Nano-Crystalline Diamonds. Due to the small grain size polishing might not be necessary for Ultra Nano-Crystalline Diamonds. These diamonds can have a surface roughness as low as 20-40nm. Because the volume fraction of grain boundaries becomes larger with smaller grain size it changes the property of the entire diamond.

3.6 Diamond ablators for target applications

The key to successful fusion is to build reproduceable targets with the required accuracy. Currently the diamond ablator is a 2 mm diameter capsule at the center of a 10 mm long × 5 mm diamond cylinder, called a hohlraum. The hohlraum has to be build out of a high-Z material like uranium to convert the laser light into soft x-rays. The target absorbs these soft x-rays and has to be built out of low-Z materials, like CH, beryllium or high density carbon (diamond). Each material has some differences in the required parameters, like the thickness of the shell. Details for CH and beryllium targets can be found elsewhere [19].

Some parameters for the ablator shell are [20]:

1. Capsule doping and thickness
2. Capsule inner surface roughness

3. Capsule outer surface roughness
4. Capsule material purity
5. Capsule spherically
6. Capsule density

A critical factor in target performance is the quality of the inner surface of the diamond shell. This is particularly true in that this surface finish cannot be improved at a later stage of fabrication. The quality of the surface is mainly controlled by two factors: mandrel precision (sphericity and defect density) and the nucleation density of the diamond [3]. The outer surface of the current shell designs has to be polished to get the required roughness.

Each of the three target materials has different characteristics for fusion. Beryllium ablates more effectively and provides a more robust implosion compared to the CH shells. On the other hand the CH targets allow optical characterization of the deuterium tritium layer [19]. Both materials have been used for fusion experiments for a long time and a good understanding of their behavior is known. Diamond is a new approach for fusion capsules with promising advantages. Compared to the other low-Z materials high density carbon may absorb 10-20% more energy, thus effectively increasing the laser energy by the same factor which makes the diamond target more robust. The higher energy efficiency of diamond targets is a consequence of diamond's higher initial density, which allows the ablator shell to be at a larger diameter after shock compression for a longer time [3].

Diamond compared to the two other materials is a new approach. Currently many shock experiments are performed at the Omega laser at the University of Rochester. These high density experiments are essential to optimize the laser pulse shape, the corresponding hohlraum temperature and the shock sequence to avoid a partially melted state while keeping the fuel entropy tolerably low [3]. Equation-of-state tables are created through these experiments and computer simulations are performed to improve the target design.

A production process for the diamond targets has been developed by the Lawrence Livermore National Laboratory and the Fraunhofer Institute für angewandte Festkörperphysik. Figure 3.6 shows the process of producing diamond targets. (a) The production starts with nearly perfect spherical and defect free silicon mandrels. Theses mandrels are manipulated by a cone shaped rotating plate. To change the axis of the mandrel there is a small notch to turn them every revolution. While they were turned a thin uniform film of Nano-Crystalline Diamond is deposited on them by microwave plasma assisted chemical vapor deposition. A batch of diamond coated Si spheres (mandrels) is shown on the right. (b) Polishing the outer surface to a nanometer-level surface finish. The one-dimensional profile shown on the right was measured around the equator of the shell with an atomic force microscope and reveals a sub-10nm RMS surface roughness finish. To decrease costs in future it is planned to grow the Ultra Nano-Crystalline Diamond with a surface finish which does not need polishing (c) Fabrication of a $5\mu m$ diameter holes through the diamond film using a diode pumped, q-switched Nd: YAG laser with

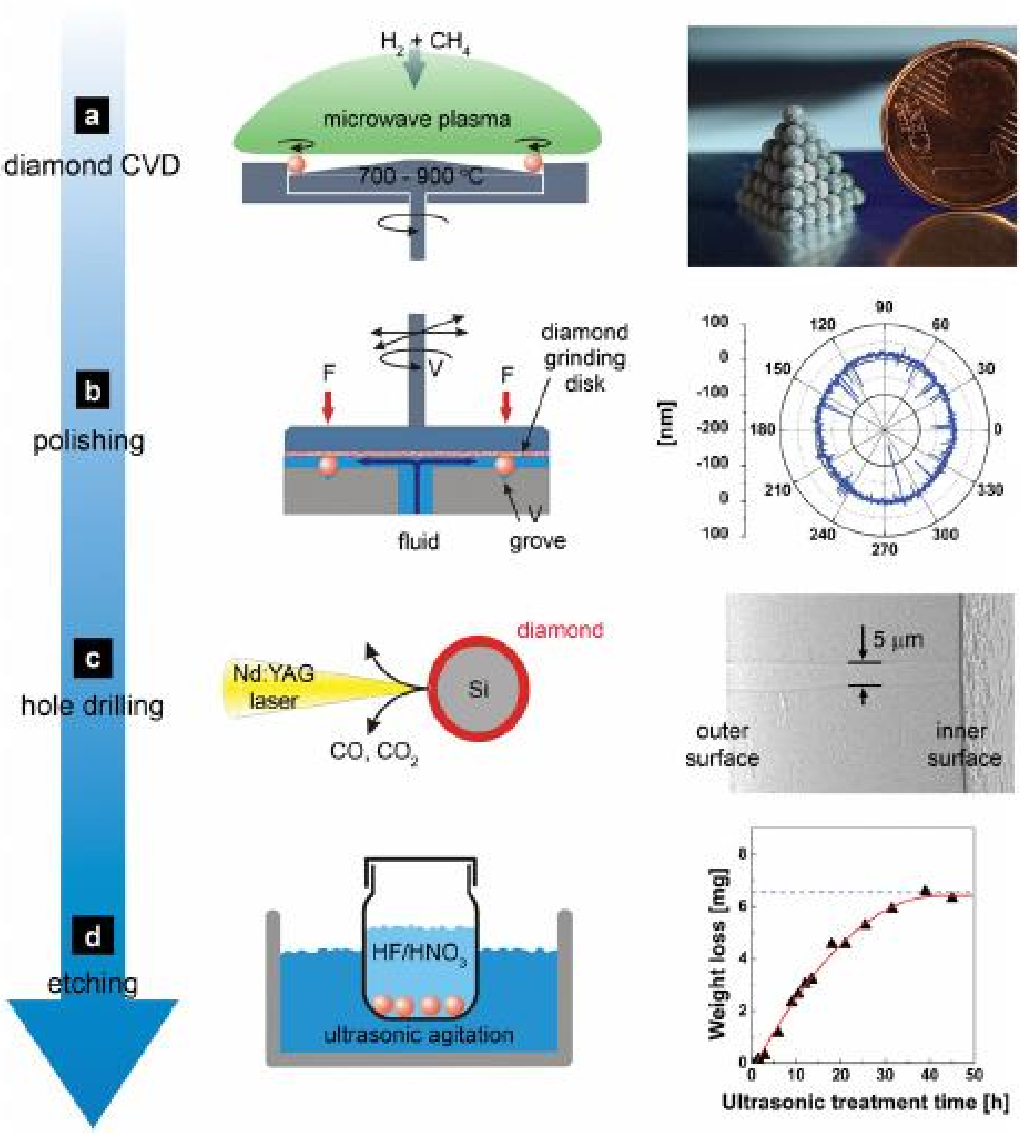

Figure 3.6: a.) shows the deposition of diamond on silicon mandrels. The plasma works as described in figure 3.5. The spheres are continuously turned during the growth process. The right side shows a batch of diamond coated silicon mandrels. b.) illustrates the polishing of the diamond coated silicon spheres. The picture on the right side is an atomic force microscope profile around the equator of the polished diamonds. The roughness is less than 10nm RMS which is within the NIF specifications. In c.) a laser drills a hole in the diamond shell only releasing CO and CO_2 gases. Holes with $5\mu m$ in diameter can be realized. d.) shows how the silicon mandrel is etched out to produce a hollow diamond sphere. The ultrasonic assisted HF/HNO_3 etch process removes the silicon mandrel within 40 hours [3]

4 kHz pulse repetition rate at an average power of 10 Watt. Only volatile products are formed. Note that the density variation produced by the $5\mu m$ hole is very small as indicated by the weak contrast of the radiograph image shown on the right. (d) Etching of the Si mandrel using an ultrasonically assisted HF/HNO_3 wet etch process. The etch rate exhibits only a very weak diameter dependence of the hole diameter indicating that the mass transport is facilated by ultrasound [3].

4 Experimental Techniques

4.1 Optical Microscopy

Microscope pictures were taken to get a first overview of the diamonds. It was verified that all diamonds were clean, homogeneous and without major scratches to perform further characterization with other instruments. Diamonds with visible surface damages were cleaned or separated from the characterization batch. A Zeiss Axioplan 2 Microscope with 100x magnification was used to obtain the pictures.

4.2 Scanning Electron Microscopy

Scanning Electron Microscopy (SEM) high resolution images have a large depth of field yielding a characteristic 3D appearance useful for understanding the surface structure of the diamonds. A narrow electron beam is generated by a cathode and scans over the sample surface. Mainly secondary electrons are detected and processed to analyze the data. For many materials sample preparation is necessary to achieve good results. Specimens must be electronically conductive and electrically grounded to prevent the accumulation of electrostatic charge at the surface. Often a thin layer of Gold or similar material is applied on the sample surface for these requirements.

For the diamond scans a Hitachi S-800 SEM was used with 10kV bias. To make the diamonds conductive a thin layer (about 20nm) of Palladium was evaporated on the surface. Results were acquired perpendicular to the beam and with the surface angled 45 degrees to the beam. All specimens were scanned with a high resolution. The smooth diamonds were scanned with a 2 μm, 5 μm and 10 μm scale. The coarse samples on a 2 μm or 5 μm scale and additionally a 10 μm and 50 μm scale.

4.3 White Light Interferometry

White Light Interferometry (WLI) is a technique to measure the topography of a surface. Optical interference is a basic technique which involves splitting an optical beam from the same light source into two separate beams - one of the beams is reflected by the sample and the other beam is used as reference. A beam splitter separates the collimated light of a white light source. The reference beam is reflected by a flat reference surface and then passed through the CCD sensor. Both beams pass through various lenses, the layout changes with the system (e.g. Twyman-Green-Interferometry, interference microscope with Mirau-Objective). Depending on the system one can introduce a phase shift into the measurement beam by moving a lens or by moving the sample stage. During this movement the distance the reference beam travels remains fixed. Due to this movement the maximum constructive interference point can be found. The CCD sensor records these coherence peaks [7, 76, 17, 61]. By using two or more different wavelengths the vertical resolution can be increased [76]. Specials programs can process this data with the distance of the movement and calculate a 3D topography of the surface. Resolutions in z-direction from 0,1nm to 1nm are typical. The 3D image contains all information needed to calculate the roughness.

Our measurements were performed with a Wyko NT1100 from Veeco with a high (50x) magnification objective. The field of view lens was 0.5x. Out of the typography diagrams the averages roughness R_a was calculated. R_a is per definition the arithmetic mean of vertical deviations of a single profile measurement [18]. To make our measurements more representative we calculated the average of several R_a measurements.

4.4 Atomic Force Microscopy

Atomic Force Microscopy (AFM) was conducted to verify the roughness measurement and to get an impression of the grain sizes. The AFM is a combination of the principles of the scanning tunneling microscope and the stylus profilometer. It incorporates a probe that does not damage the surface [5]. A sharp probe, scanned raster-fashion across the sample, is employed to detect changes in the surface structure on the atomic scale [67] Basically an AFM consist of a cantilever with a sharp tip (the tip radius of curvature is about 10nm). By bringing the tip into the proximity of the sample surface forces between the sample and the tip lead to deflection of the cantilever. This deflection is measured by laser reflection on the cantilever by a photodetector.

Measurements were conducted in two different modes: Contact Mode and Acoustic AC Mode. In Contact Mode AFM, interatomic van der Waals forces become repulsive as the AFM tip comes in close contact with the sample surface. The force exerted between the tip and the sample in contact mode is on the order of about 0.1-1000nN [2]. Acoustic AC Mode (AAC mode) is an oscillating technique that is less destructive than contact mode. AAC mode excites the cantilever by vibrating the piezo where the cantilever holder is attached [1]. A Molecular Imaging AFM (today agilent technologies) was used for the diamond samples. All measurements in the lower resolution range were performed in contact mode with a nanosensors tip. Particularly for the coarse samples the contact mode lead to good results. For the small sized grained samples; both techniques were used.

4.5 Near Edge X-ray Absorption Fine Structure

Near edge X-ray absorption fine structure (NEXAFS) is an electron spectroscopic technique to determine carbon hybridization and Hydrogen content in carbon films. NEXAFS measures the unoccupied density of states above the Fermi energy by resonant absorption of X-rays photons. This requires a tunable x-ray source, like a synchrotron. X-rays with energy equal or higher than the absorption edge are absorbed resulting in a core level hole and the emission of a photoelectron. The resulting core hole is filled with an electron from another shell. This leads to the emission of a detectable fluorescent photon or an Auger electron (figure 4.1) [67].

Depending on the requirements different measurements can be done for NEXAFS. For surface measurements the Auger electron are detected. Due to the complexity of detecting auger electrons often the total electron yield is measured. The absorption of an X-ray at the core level leads to the emission of a photoelectron which can be easily measured. Detecting fluorescent photons gives the best spectrum of a bulk sample [67]. In this case the total fluorescent yield is plotted versus the photon energy. Otherwise the total electron yield is plotted versus the photon energy.

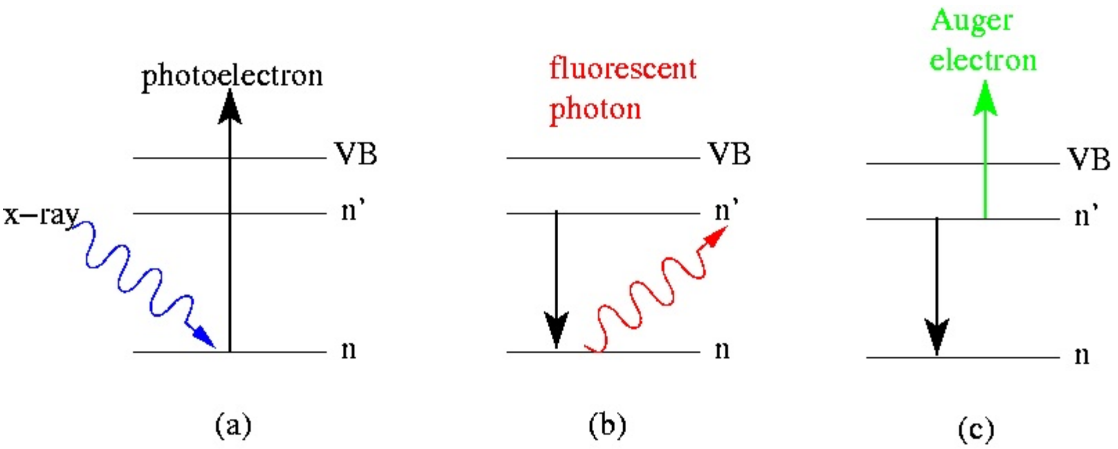

Figure 4.1: All three cases start with a photoabsorbtion of a x-ray into the core level 'n' followed by the emission of a photoelectron. By measuring the total electron yield most of the electrons are the electrons described in a.) which can be easily detected as electron current in the sample. In case b.) or c.) the core hole electron jumps into an unoccupied state 'VB' and the core hole is filled by an electron from the occupied state 'n". Emitting a fluorescent photon is shown in b.). c.) illustrates the emission of an Auger electron

To analyze the the results for carbon a highly oriented pyrolithic graphite (HOPG) and a optical diamond were used as reference standards. The HOPG shows two peaks which are associated with the carbon double bonds, the π^* and σ^* peaks. Diamond has just one σ^* peak for the carbon single bond [9]. The estimate the Hydrogen in the samples the CH content can be acquired at the left shoulder of the diamond peak.

The NEXAFS results in this thesis were obtained at the Advanced Light Source synchrotron at the Lawrence Berkeley National Laboratory in Berkeley, California. Unfortunately a appropriate sample holder with integrated heating for the diamonds was missing. Due to the lack of the heating the cleanness of the diamonds could not be assured. Especially by comparing the measured results with the reference samples the plots are not within the expectations. Surprisingly the best results were obtained by using the electron attractive wire with +1000V before the electron repellent grid -300V. Probably some electrons were accelerated so much that they made it through the repellent grid. This indicates that our results are a mix of fluorescent photons and auger electrons. Measurements without the electron attractive wire do not look useful at all. To acquire better results a sample heater and holder has to be fabricated for the diamonds.

4.6 Raman Spectroscopy

Raman spectroscopy is a useful technique for the identification of a wide range of substances. It is a straightforward, non-destructive technique requiring no sample preparation. Raman spectroscopy involves illuminating a sample with monochromatic light and using a spectrometer to examine light scattered by the sample [34]. Mostly lasers are used for this purpose. The physical concept behind the process is called the Raman effect. The incident light is inelastically scattered from an atom or molecule. By exciting the molecule or atom from the ground state to virtual energy state. This virtual energy state is unstable and the molecule or atom relaxes but returns to a different rotational or vibrational state. The emitted photon now has a different frequency than the incident photon. Mostly this energy is lower which is called Stokes-Raman-Scattering, if the energy is higher it is Anti-Stokes-Raman-Scattering. These photons are detected as well as the shift in energy which is equal to the vibrational change of the molecule. Because of the vibrational changes Raman spectroscopy is a subcategory of vibrational spectroscopies.

Similar as in the NEXAFS measurement the goal is to get an estimation of the graphitic carbon within the diamond samples. Pure diamond has on sharp peak at 1332 cm^{-1}, which is the characteristic diagnostic feature for diamond [29]. An additional peak for diamond can be found at 2450 cm^{-1} which is not observed with every instrument [29]. Graphite has various different bands compared to diamonds. An overview about bands visible in graphite can be found elsewhere [27]. For the spectral region between 1000 cm^{-1} and 1800 cm^{-1} there are two important major bands. One peak is around 1580 cm^{-1} which is the G-Band. When disorder is introduced into the graphite structure, the bands broaden and an additional line is found at about 1357 cm^{-1}, the so called D-Mode [26]. A broad band around 1500-1550 cm^{-1} was also noticed in several cabon-based materials and was associated with amorphous sp^2-bonded forms of carbon [29, 26]. Additionally a D' mode at 1615 cm^{-1} is sometimes slightly visible. A small hump at 1150 cm^{-1} is due to trans-polyacetylene [53, 13]. The intensity of the graphite spectrum is 50 times that of the diamond spectrum, because of the scattering efficiency for graphite. The Raman spectrum is a very effective means of detecting percentage levels of graphitic carbon in diamond films but is not a sensitive test for diamond in the presence of other types of carbon [29]. Nevertheless these peaks are found with a laser wavelength of 514,5nm.

Several techniques were developed to estimate the quality of the diamonds. Lespade P. et al. showed four characteristics to judge the quality in [36], which are commonly used (e.g. [29]).

1. the wavenumber of the G band

2. the band with of the G band
3. the D/G integrated intensity ratio
4. the band with of the second order phonon at 2700 cm^{-1}

Sails R. S. uses a similar technique to obtain some diamond indices in [59], which has an higher emphasis on the diamond peak. Somehow everybody does the curve fitting for the raw data different. In [26] two Lorentzian and a broad Gaussian fits are used, [58] uses four Lorentzian shaped bands and one Gaussian fit, [13] used four Lorentzian fits, [14] uses just two curves fitted with Gaussian and Breit-Winger-bands., [59] fits with a mixed Lorentzian-Gaussian function the diamond band and all non-diamond bands with pure Gaussian functions. Further parameters influence the results of the final analyzed curves. Lipp M.J. claims that the laser heating effects dramatically affect the measured Raman spectra [40]. Probably the parameter with most influence on the appearance of the results is the used laser wavelength (λ) reported by [27, 13]. λ influences most of the peaks differently, the diamond peak at 1332 cm^{-1} and and the G-Band (1580 cm^{-1}) stay the same. All other bands move with higher λ to lower wavenumbers.

The measurements for the diamond films were performed as a macro Raman spectroscopy. The beam size was about 200 μm and the incident beam hits the specimen in a small angle and backscattered light is detected normal to the surface. The beam was generated by an Argon Ion laser with λ = 457,94 nm. Unfortunately all the literature mentioned above uses higher wavelengths which make the data analysis more challenging.

To fit these results a linear baseline was subtracted that the ordinate values are zero at 1200 cm^{-1}. All the peaks to related to the sp^2 content and the diamond peak were within this region. In this case the curves were best fitted by a Lorentzian fit for the diamond peak and the graphitic components by a Gaussian function. Unfortunately no real reference data was found for this laser wavelength with Nano-Crystalline Diamonds.

4.7 Elastic Recoil Detection Analysis

Elastic Recoil Detection Analysis (ERDA) is an ion beam technique to determine the elemental concentration of light elements in a specimen containing a high concentration of heavier elements. Here we determined the Hydrogen content. ERDA is similar to Rutherford Backscattering (RBS). RBS involves measurements of the energy distribution of energetic ions (usually MeV light ions such as He^+) backscattered form atoms within the near-surface region of solid targets [6]. Backscattering cannot detect light target constituents. However, forward scattering geometries like ERDA can be used to advantage for the detection of atoms that are forward scattered which emerge after collisions by the heavier incident ions [6].

The system used for measuring the Hydrogen content of the diamonds consists of a 4 MV ion accelerator generating a 3 MeV $4He^+$ ion beam. The samples were mounted in a vacuum chamber. θ the angle between the incident ion beam and the forward scattered ions was 75°. ψ the angle between the incident ion beam and recoiled light nuclei was

75,59°. A Mylar stopper foil is placed in front of the detector to block out the scattered incident ions but allow the lighter atoms which suffer considerably less energy loss to pass through to the detector [6]. A depth profile was measured with peaks for Silicon, Nitrogen, Oxygen, Gold and Carbon. The Nitrogen, Silicon and Gold peaks were barely visible. The focus of the following analysis is the carbon peak area.

4.8 Fourier Transform Infrared Spectroscopy

Fourier Transform Infrared Spectroscopy (FTIR), a vibrational spectroscopy, is used to identify compounds and characterize sample compositions. Infrared spectra are often measured in transmission and the absorption of the incident beam is measured as a function of the wavelength. By investigating these absorption spectra details about the molecular structure are revealed. The Hydrogen active frequencies are from 2800-3200 cm^{-1}.

As already mentioned for the ERDA (pg. 24) Hydrogen is an impurity in the diamond that plays a major role in controlling various characteristics of the material. In contrary to the ERDA measurement the FTIR spectroscopy only identifies bonded carbon, but samples the complete film thickness. The deconvolution of the spectra in the three-phonon region (2700-3150 cm^{-1}) shows a number of vibration modes corresponding to sp^nCH_n phase of carbon. K.M. McNamara et al. [43] and M.S. Haque [22] propose two similar approaches to measure the Hydrogen content in this region. Basically the integrated intensity of the entire peak in this three-phonon region is proportional to the Hydrogen concentration in the diamond.

B. Dischler [12] describes the vibrations frequencies which can be found in the above mentioned region. sp^2CH_2 has its vibrational frequencies at 2972 and 3025 cm^{-1} in most of the literature just the latter peak is observed within the spectra [65, 25]. The intensities below 3000 cm^{-1} can be attributed to sp^3CH groups, above 3000 cm^{-1} to sp^2CH groups. The Hydrogen bonded to sp^2 is considerably small compared to sp^3 since the sp^2 content of the samples is already low. Other sp^2CH peaks are not visible in most diamonds either. The main peaks are at 2850 cm^{-1} and 2920 cm^{-1} which are associated with the symmetric and asymmetric stretching band of sp^3CH_2. The bands at 2880 cm^{-1} and 2960 cm^{-1} on the other hand are due to symmetric and asymmetric stretch modes of sp^3CH_3 groups. Nitrogen and Hydrogen bonded CH peaks are at the lower wavelength NCH_3 at 2820 cm^{-1} and OCH_3 at 2832 cm^{-1} [65]. On the other hand C.J. Tang shows that the 2828 cm^{-1} $O - CH_3$ peak is not related to oxygen. It shall be more related to Hydrogen bonded to some kind of structural defect of CVD diamond like twinning or stacking faults [64]. These are the major 7 bands which are used in the literature to fit the three phonon region. Theoretically there are a more vibrational bands but are mostly not visible in the raw data. Further information about these bands can be found elsewhere [12]. In contrast to the Raman data shown on page 41 the infrared data can be fitted with Gaussians as suggest by B. Dischler [12].

Additional to the Hydrogen characterization more data can be obtained from the interferograms before the fourier transformation. The fringe pattern of the interferogram can be used to calculate the refraction index or the thickness of specimens. Moreover the refraction index can be proportional to the density of the material. T.J. Clark et. al. proposes a formula to calculate the thickness of different films by the fringe pattern [10].

$$t = \frac{N(\lambda_1 \lambda_2)}{2(\lambda_1 - \lambda_2)(n^2 - sin^2\theta)^{\frac{1}{2}}} \tag{4.1}$$

$N(\lambda_1\lambda_2)$ is the number of fringes between the beginning wavelength λ_1 and the ending λ_2 ($\lambda_1 > \lambda_2$). n is the refractive index of the film and θ the angle between the incident beam and the line normal to the surface. Since the thickness of the diamond samples is already known, equation 4.1 can be transposed to the refraction index. Several values of the refractive index can be found in the literature. X.H. Wang proposes a refractive index of 2,41 to 2,49 [68], T. Sharda values between 2,33 and 2,35 [60] and F. Peter published a formula with refractive indices above 2,38 [52]. For some materials there is a dependency of the refractive index with the density. A formula like

$$\frac{n-1}{\rho} = const. \tag{4.2}$$

can be found online. By assuming that the constant is the same for diamonds the density can be calculated for various diamonds with this formula. As reference the properties of optical diamond were used ($n = 2,4176$ and $\rho = 3,52\frac{g}{cm^3}$). Unfortunately these values do not seem to be appropriate for our diamonds since the determined density was above 4 $\frac{g}{cm^3}$. To validate this approach to obtain the density a better reference sample is necessary which can be actually measured. Unfortunately a standard with known Nano-Crystalline Diamond properties was not available.

4.9 Transmission Electron Microscopy

Transmission Electron Microscopy (TEM) is one of the most accurate methods to determine the grain size distribution of bulk diamond [54]. A special sample preparation is necessary to get a small thin slice out of the bulk diamond. Hit by an electron beam the prepared specimen is measured in transmission. Depending on the magnification results can be obtained by electron absorption within the sample or by complex wave interactions that modulate the intensity of the image. Special analysis is required to obtain useful information out of it. Grains are clearly visible on the images.

Unfortunately the TEM results were not ready with the due date of this thesis. The complex sample preparation needs highly qualified experts to extract the diamond slice out of the bulk material. Particularly a focus ion beam extraction was avoided to not influence the measured surface with the ions. An expert who could extract the sample without the focus ion beam technique was not found on time. Accurate grain size distribution information is missing in this thesis.

4.10 Density

The Density of the diamond was measured to determine the mass per volume fraction of the diamonds. To obtain the density the Archimedes' principle was used. This means to measure the weight within two different surrounding mediums which are water and air. The weight of the displaced fluid is directly proportional to the volume of the displaced fluid. Knowing the displacement and the density of the displaced fluid the density can be easily calculated - shown in equation 4.3 with air and water as fluids.

$$\rho = \frac{(m_{air} * \rho_{water}) - (m_{water} * \rho_{air})}{m_{air} - m_{water}} \tag{4.3}$$

First the diamonds were weighed in air (a density of $\rho_{air} = 1.2041 \frac{kg}{m^3}$ at 20°C was used for the calculations). Afterwards a special set up was installed into the lab balance to measure the weight of the samples in water. About three drops of soap were added to the water to decrease the surface tension. A basket attached to the transducer of the balance was used to obtain the weight under water. Since the density of water is more temperature dependent, the appropriate density was used for every temperature. To increase the accuracy the measurement was repeated at least 3 times. Due to some difficulties in the beginning with too light specimens a half wafer was used from each Condor series. There are still difficulties to measure the density of light samples with less than 0,02g. Particularly measurements under water tend to creep to lower values for more than one hour which cannot be explained yet.

4.11 Three point bending test

The three point bending test was used to obtain the Young's Modulus of materials. This physical property is especially dependent on the grain size and graphite content of the diamond. The grain boundaries weaken the material. The goal is to link these values to the diamond quality. For this test only the elastic part was determined which means reversible bending; Figure 4.2 shows the basic test set up. The sample is prepared in a rectangular shape and mounted on two sharp edges. The edges have a defined distance. In the center of the specimen a tip bends the sample while the traveled distance and the force of the tip is recorded.

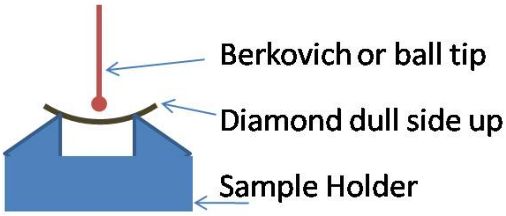

Figure 4.2: describes the diamond being bended by a tip. In case of the Berkovich tip a transducer measures the force and the traveled way. On the other hand the ball tip is moved with defined steps by a linear stepper motor, the force is indirectly determined by a balance. The sample geometry, the deflection and the force are all the necessary parameters to calculate the Young's Modulus

Two different set ups were used. First measurements were performed with a Hysitron nanoindenter. The sample holder was fixed by magnets and the proper position was determined with an integrated coordinate microscope camera. Maximal loads between 1500 and 2500 μN were used with a dull berkovich (triangular geometry) tip. The second approach was with an accurate linear motor pushing with a ball tip on the specimen. 2 μm steps slowly increased the load on the diamond. The sample holder was positioned onto a balance and the change in increasing weight was logged by a computer. To get a force the weight has to be multiplied with the earth's gravitational attraction. Basically both approaches should give similar load curves which can be used to calculate the Young's Modulus. The basic equation for deflection [18] is used:

$$y_{max} = \frac{F * L^3}{48 * E * \frac{b*t^3}{12}} \tag{4.4}$$

Transformation of equation 4.4 to the Young's Modulus (E) leads to:

$$E = \frac{F * L^3}{y_{max} * 4 * b * t^3} \tag{4.5}$$

Hence $\frac{F}{y_{max}}$ is the slope and all the other factors are only geometry constants the Young's Modulus can easily be calculated.

4.12 X-Ray Diffraction

X-ray diffraction is a method which gives a unique fingerprint for crystalline materials. A sample is radiated with monochromatic x-rays, the reflection of these x-rays at the sample leads to constructive and destructive interferences. By changing the angle between the incident beam and the detector a unique pattern can be measured. Bragg's law further describes these patterns:

$$2 * d * \sin(\theta) = n * \lambda \tag{4.6}$$

d is the distance between diffraction planes within a crystallite. Incident x-rays with angle θ to the surface hit the electrons of the different diffraction planes at various path differences. By geometry a beam at a lower plane with the distance d to the upper plane has to travel $2 * d * \sin(\theta)$ longer distance. To obtain constructive interference this value has to be an integer multiplied with the wavelength. The wavelength has to be similar to the d unit cell spacing to achieve the constructive interference conditions. By changing the angle θ a unique pattern for each material can be obtained and hence the lattice and the distance between the atoms can be determined.

The measurements performed in this thesis were done with a Bragg Brentano diffractometer. A X-ray source generates monochromatic x-rays which are focused on the specimen and reflected onto the detector. The measurement was performed in reflection. The detector and generator are located on the diffractometer circle and the sample is in the center of this circle. The detector is moved twice as fast as the beam generator. This is called a $\theta 2\theta$ scan. To mitigate noise slits are used to limit the spread of the beams.

For a perfect crystal the grain size can be identified with the equation from P. Scherrer [78] for grain sizes less than 0.1 μm. This formula utilizes the diffraction patterns obtained by a $\theta 2\theta$ scan. The width of the peaks is linked to the grain size of the crystals within the samples. The broader the peaks the smaller the the crystals.

$$t = \frac{K * \lambda}{B * \cos(\theta_B)} \tag{4.7}$$

K represents a constant dependent on the crystallite shape. In the literature this value is between 0.89 and 0.94. A reference value should be obtained by a different measurement like TEM to verify the K-constant. λ is the wavelength of the x-rays, B is the full with at half max of the peak and θ_B is the Bragg angle. Unfortunately not only the crystallite size influences the width of the peaks. Additionally strain, twist and tilt has an influence as well as the instrument parameters itself [66]. Several other approaches exist to estimate the grain size, like Williamson-Hall or Warren-Averbach, details can be found elsewhere [32, 77].

A pole figure is scanned by measuring the diffraction intensity of a given reflection (x-ray tube and detector are fixed, 2θ is constant) at a large number of different orientations of the sample. Angle ϕ and χ describe the rotation on the normal axis of the sample and tilting of the sample.

5 Results and Analysis

Nine different diamonds will be analyzed in this thesis. All of them were grown under different conditions. The changing parameters are the temperature and the Methane concentration during the growing procedure and some were seeded with nano-seeding. The temperature series consists of three diamonds (#51, #58 and #59) grown at 770°C, 830°C and 890°C with a constant Methane concentration of 3%. The Methane series (#53-#56) has four different Methane concentrations at 2%, 2.5%, 4% and 5% all grown at temperatures between 830°C and 860°C. Additionally there are two nano-seeding diamonds (#60 and #61) one with 4% Methane and 850°C and the other one has high growth temperature and high Methane concentration.

5.1 Surface morphology

To characterize the surface morphology the optical microscope, the SEM, the WLI and the AFM were used as described in the experimental section (page 20).

The optical microscopy results allowed to roughly group the diamonds with different surface roughnesses:

- NCD with smooth surfaces like figure 5.1a: #53 ($4\%CH_4, 850$ ℃), #54 ($5\%CH_4, 830$ ℃), #60 ($4\%CH_4, 850$ ℃, nanoseeding) and #61 ($5\%CH_4, 890$ ℃)
- Fine grained with medium smooth surfaces like figure 5.1b: #51 ($3\%CH_4, 830$ ℃) and #59 ($3\%CH_4, 890$ ℃)

Table 5.1: Growth parameters diamonds

Diamond	Duration [hr]	Rate [$\frac{\mu m}{hr}$]	CH_4 [%]	Temperature [°C]	Thickness [μm]
#51	80	0.3835	3	830	30,68
#53	100	0,4407	4	850	44,07
#54	100	0.4061	5	830	40,61
#55	100	0.394	2	850	39,40
#56	100	0.4206	2.5	840	42,06
#58	100	0.3466	3	770	34,66
#59	100	0.4217	3	890	42,17
#60	100	0.4431	4	850	44,31
#61	100	0.3683	5	∼890	40

- Coarse grained surfaces like figure 5.1c: #55 (2%CH_4, 850 ℃), #56 (2.5%CH_4, 840 ℃) and #58 (3%CH_4, 770 ℃)

On the top right corner of many of the pictures a reflection of the light from the room is visible. The high magnification of the microscope lead to a small focus depth of the pictures. Most of the samples were not perfectly flat and parts of the pictures are out of focus due to this effect. To get accurate surface roughnesses and better focus depth further experiments were performed with different techniques. Atomic Force Microscopy (pg. 36), Scanning Electron Microscopy (pg. 31) and White Light Interferometry (pg. 33) were conducted to obtain more accurate results.

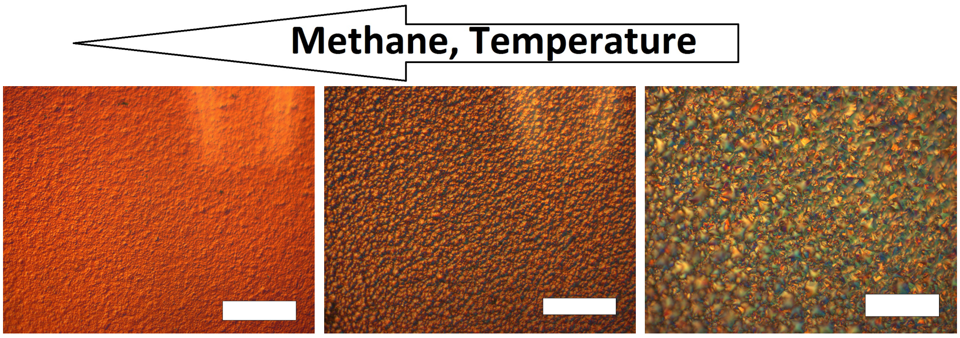

(a) #54 (b) #51 (c) #55

Figure 5.1: 5.1a shows #54 (5%CH_4, 830 ℃) the sample with the higest Methane concentration and a medium temperature. 5.1b #51 (3%CH_4, 830 ℃) is a sample with medium temperature and medium Methane concentration. 5.1c #55 (2%CH_4, 850 ℃) has a low Methane concentration and medium temperature. All samples have a 100 μm scale in the corner.

The microscope images show that the smoothness can be controlled by the temperature and Methane concentration. Samples with a higher temperature or Methane feed gas concentration had a smoother surface. No visual differences in roughness of the diamonds grown with Nanoseeding compared to the high Methane series were visible. The Methane series basically covers all visible roughness differences of our diamonds. Most of the following data analysis focuses on the Methane series.

Figure 5.2a and 5.2b show the obtained SEM results of #54 (5%CH_4, 830 ℃) and #55 (2%CH_4, 850 ℃). The beam was perpendicular in this case. Both images have the same scale of 5 μm. #54 (5%CH_4, 830 ℃) shows only small grains and it is almost impossible to estimate the grain size since the surface is so smooth. In contrast #55 (2%CH_4, 850 ℃) where the grains are clearly visible. A rough estimation of the grain size was performed by measureing the crystallite size in the SEM images. These results are shown in figure 5.3. As expected the higher the Methane concentration is the smaller the grains.

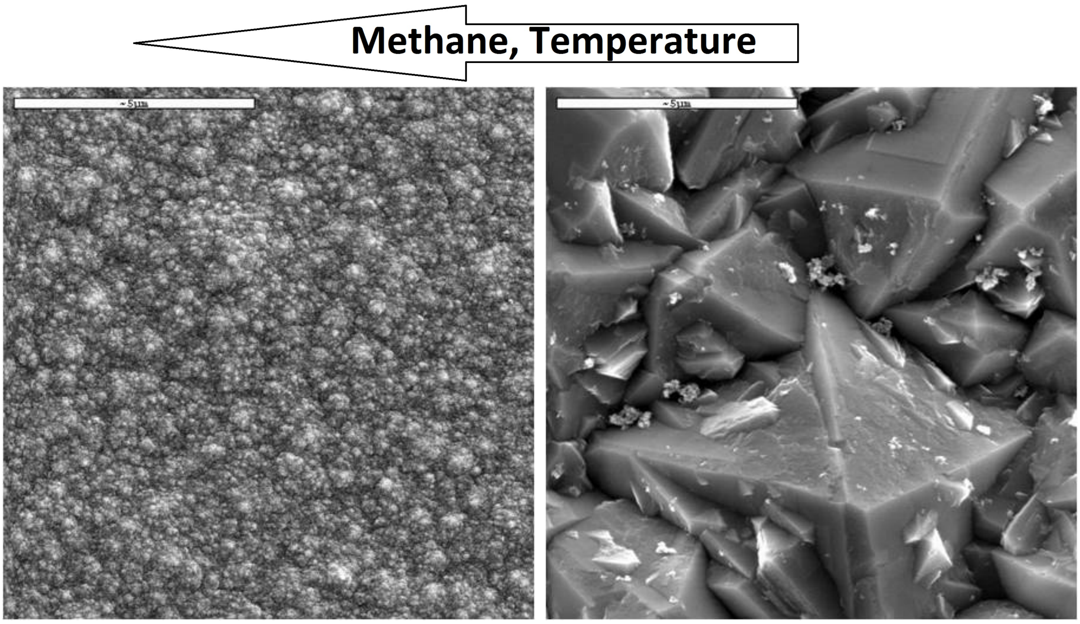

(a) #54

(b) #55

Figure 5.2: SEM images of #54 ($5\% CH_4, 830$℃) (5.2a) and #55 ($2\% CH_4, 850$ ℃) 5.2b. (5.2a shows a fine grain structure in contrast to 5.2b where one can easily see the crystallites. Both pictures have a 5 μm scale bar.

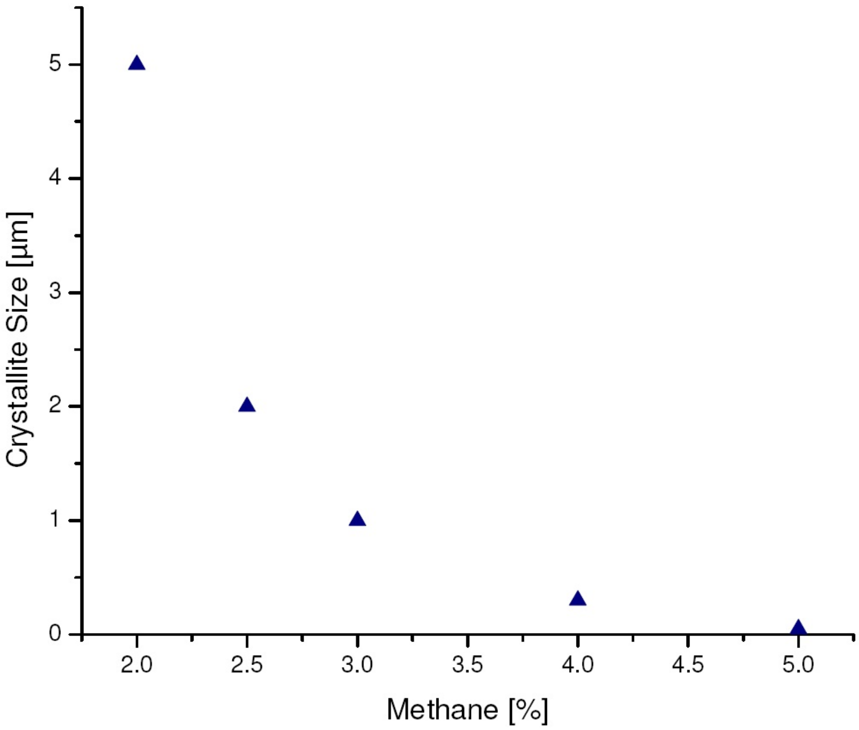

Figure 5.3: The grain size was estimated by measuring the crystallite size of the SEM pictures. All samples were in the medium temperature range (830-850℃) with different Methane concentrations (#51, #53-#56). The grain size decreases with increasing Methane concentration.

These White Light Interferometry roughness values are in good agreement with the three groups of the microscope pictures . Comparing both pictures 5.4a shows that #54 ($5\% CH_4, 830$ ℃) has much smaller grains which build up to sharp peaks. #55 ($2\% CH_4, 850$ ℃) (figure 5.4b) shows bigger grains and the peaks build more clusters with less slope.

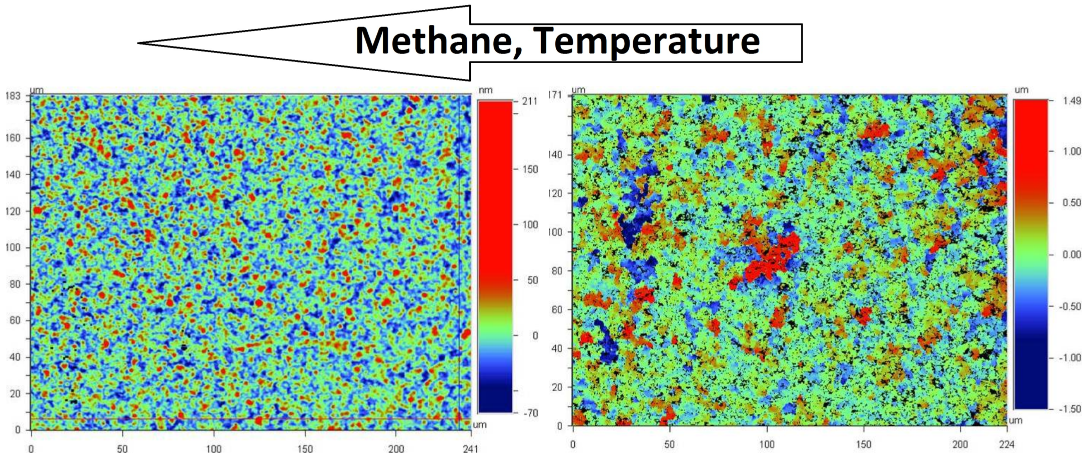

(a) #54 (b) #55

Figure 5.4: Figures 5.4a and 5.4b are two representative white light interferometry measurements. The #54 (5%CH_4, 830 ℃) topography image 5.4a has a size of about $241 \times 183\mu m$ the depth scale is in nm. #55 (2%CH_4, 850 ℃) is a bit smaller $241 \times 171\mu m$ and the depth scale is three magnitudes higher in μm. Blue represents the lower parts of the surface and red are the peaks.

Plotting the roughness versus the Methane concentration shows a clear dependency. Only the Methane series is shown in figure 5.5. The graph shows that the smoothness of the diamond surface does not increase significantly after 4% of Methane. #53 (4%CH_4, 850 ℃) and #54 (5%CH_4, 830 ℃) almost have the same roughness. The three diamonds on the left side of the graph (#55 (2%CH_4, 850 ℃), #56 (2.5%CH_4, 840 ℃) and #51 (3%CH_4, 830 ℃) show a roughness-Methane concentration dependency. A similar behavior can be identified with the temperature series. Increasing the temperature above 850°C does not show any improvement in roughness anymore.

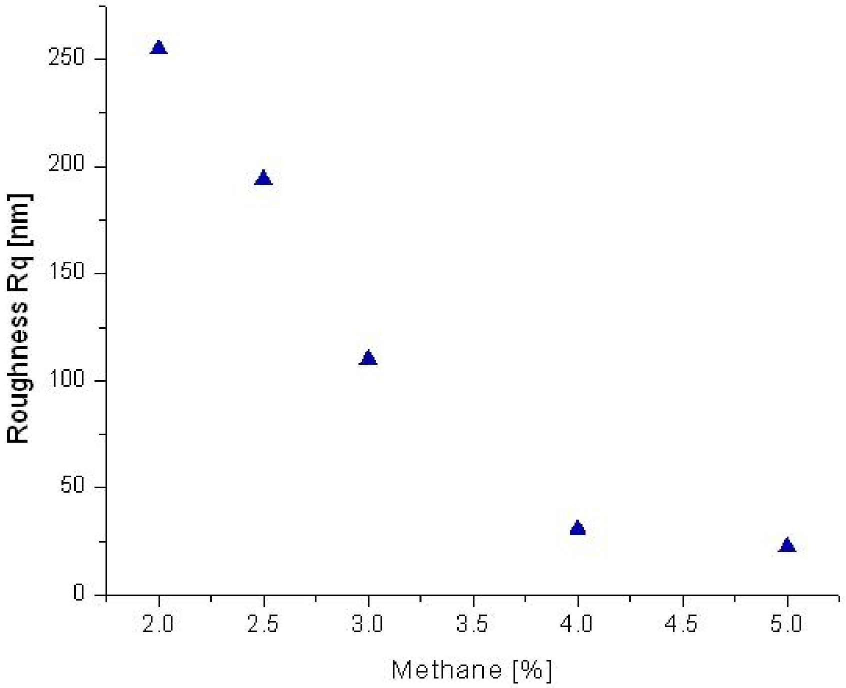

Figure 5.5: shows the roughness vs. the Methane concentration. The higher the Methane the smoother the surface. All samples were in the medium temperature range (830-850°C) with different Methane concentrations (#51, #53-#56).

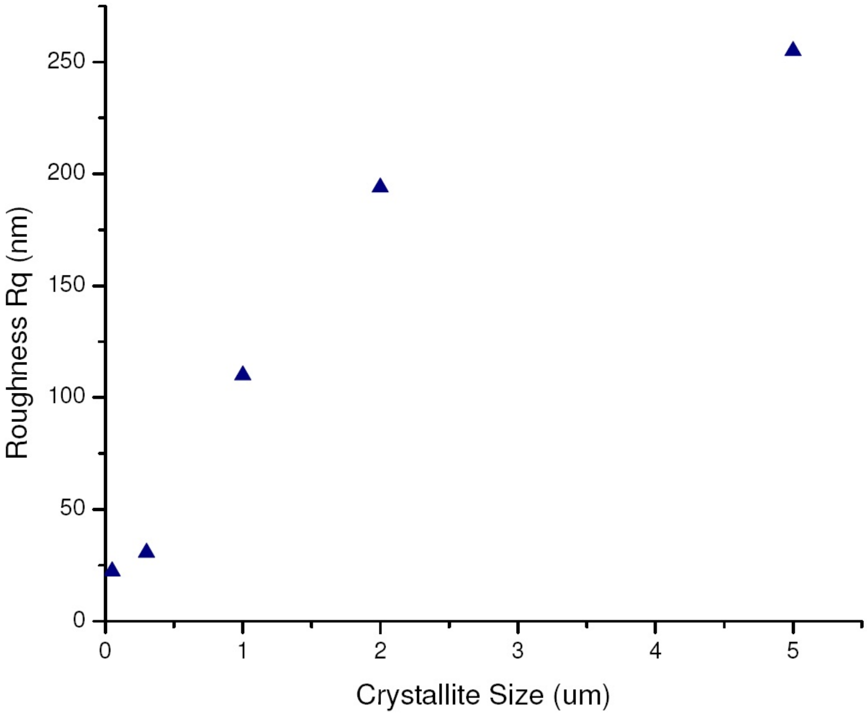

Figure 5.6: shows the roughness vs. the grainsize. The smaller the grains the smoother the surface. All samples were in the medium temperature range (830-850℃) with different Methane concentrations (#51, #53-#56).

Figures 5.7a and 5.7b represent the AFM results. #54 ($5\% CH_4, 830$ ℃) only show tiny bright areas which represent sharp peaks. #55 ($2\% CH_4, 850$ ℃) already shows the structure of the grains. A rough estimation of the crystallite size can be obtained from the coarse diamond samples by the AFM pictures. These results basically confirm the WLI result. The AFM Software PicoImage provides a tool to obtain roughness values of the samples. In contrast to the WLI results the surface roughness S_q was calculated as root mean square values in table 5.2. Comparing these results with the SEM figures 5.2a and 5.2b the results can be verified.

Table 5.2: Roughness R_a by WLI and S_q by AFM

Diamond	Methane [%]	Temperature [°C]	Roughness [nm] WLI	Roughness [nm] AFM
#51	3	830	110	97.3
#53	4	850	30.7	55.7
#54	5	830	22.4	39.5
#55	2	850	255	411
#56	2.5	840	194	338.7
#58	3	770	334	306
#59	3	890	77	118.7
#60	4	850	19	43.8
#61	5	~890	missing	34.7

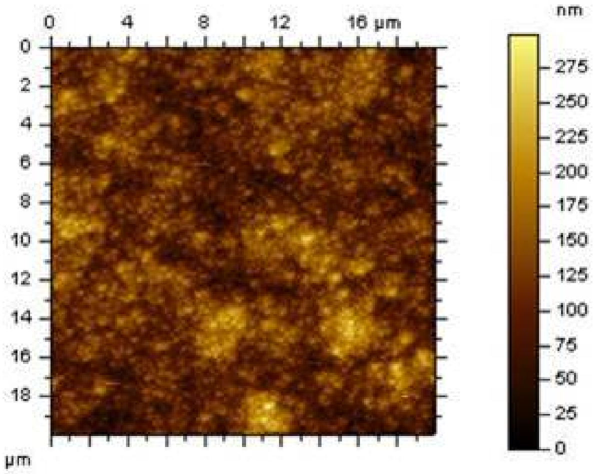

(a) #54

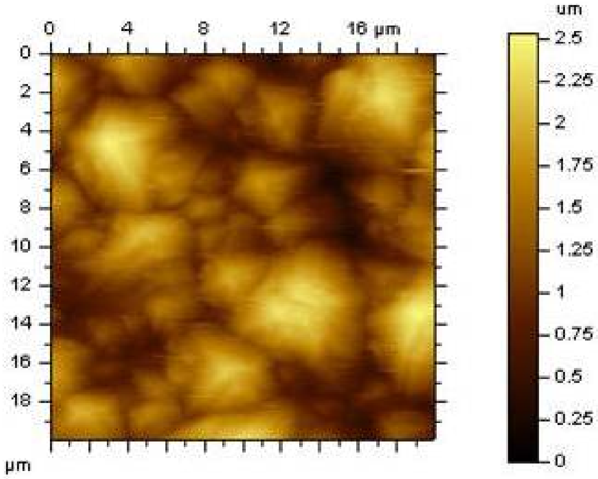

(b) #55

Figure 5.7: Both images are $20\mu m$ squares. The darker the picture the smoother the surface. Sample 5.7a #54 ($5\% CH_4$, 830 ℃) looks similar to the SEM result of the same sample on page 32. Both show a smooth surface. 5.7b #55 ($2\% CH_4$, 850 ℃) is similar to the previous SEM images as well. It shows big bright spots with peaks upto 2.5 μm similar to the coarse grains of the SEM image 5.2b.

As already seen in table 5.2 the results are much higher than the WLI values. Plotting the AFM outcomes of the roughness versus the Methane concentration (figure 5.8) leads to a similar curve as the WLI graph which is shown for comparison. Except #51

($3\%CH_4, 830$ ℃) does not match with the curvature of the WLI results. S_q is higher than R_a of the AFM results. This can be explained by the scanning technique of the AFM and the tip size. Table 5.2 summarizes these results

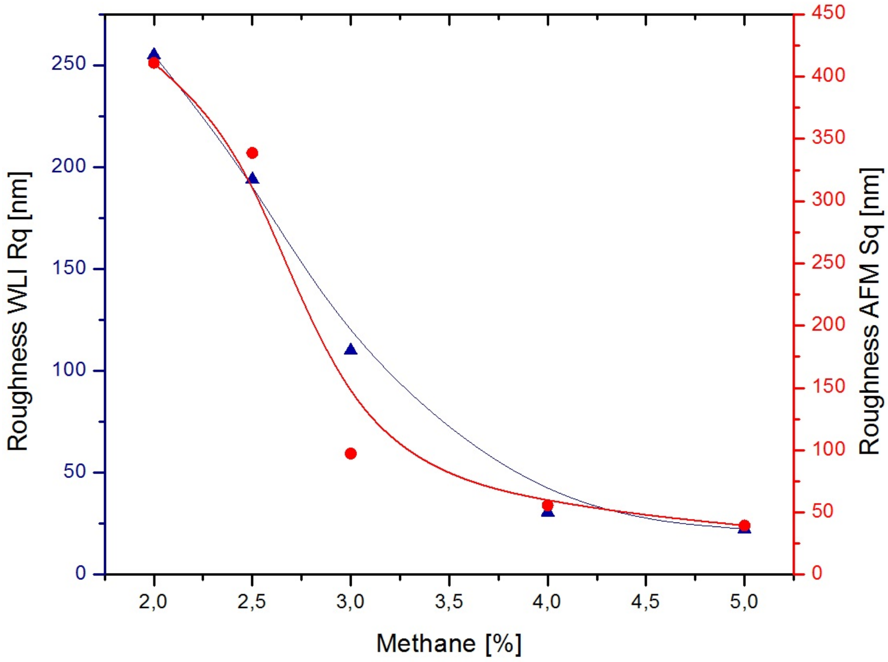

Figure 5.8: Two different roughness measurements are compared vs. the Methane concentration. The WLI results show a curve with less slope compared to the AFM measurements. The roughness influence seems to be less for Methane concentrations above 4%. Diamonds of the medium temperature range (830-850℃) with different Methane concentrations (#51, #53-#56).

5.2 Chemical composition

This section consist of the NEXAFS, Raman spectroscopy, ERDA and FTIR spectroscopy to determine the sp^2 and sp^3 ratio and hydrogen concentration.

Due to the explained circumstances above (page 22) a quantitative analysis of the NEXAFS data was not possible and it was just enough time to measure the Methane series at the synchrotron. A by eye estimation shows the mentioned graphite peaks at about 285 eV in figure 5.9. #55 ($2\%CH_4, 850$ ℃) seems to have lowest sp^2 hybridized carbon (graphite) followed by #56 ($2.5\%CH_4, 840$ ℃) and #53 ($4\%CH_4, 850$ ℃). #54 ($5\%CH_4, 830$ ℃) has the highest peak and has additionally a small shoulder for the CH content visible as well as #53 ($4\%CH_4, 850$ ℃). The diamond peak at about 289 eV shows the same intensity for all of the measurements. The σ^* peak for the graphitic double bonds is not visible within these spectra, it should be around 292 eV. An advantage of NEXAFS carbon hybridization measurements is that the intensities of the peaks proportional to the real values which is different to Raman sepctroscopy. The peak sp^2 height at 285 eV was measured and plotted versus the Methane concentration in figure 5.10. Since sp^2 carbon is mainly found within the grain boundaries this result is expected.

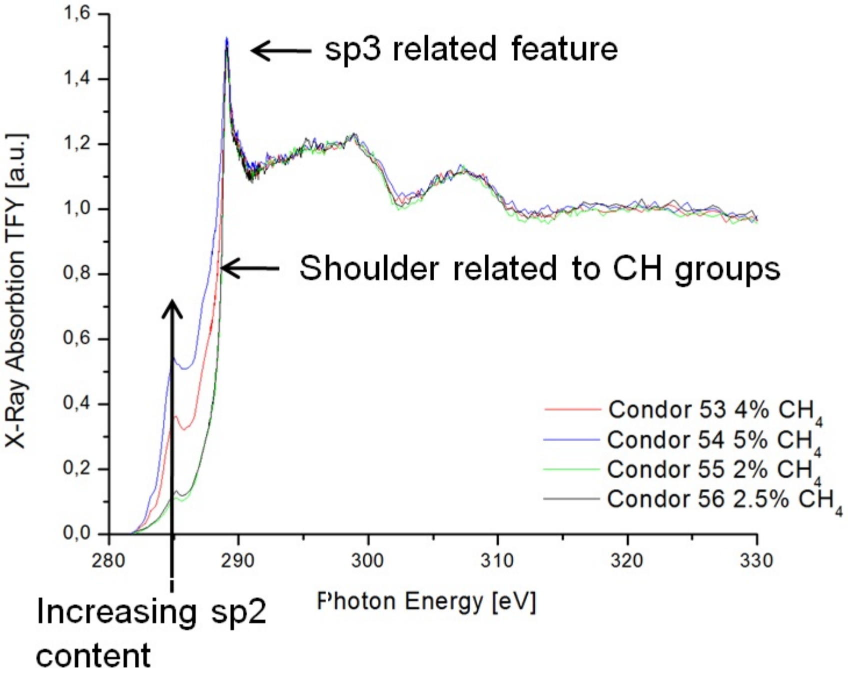

Figure 5.9: Shows an estimation of the sp_2, sp_3 and Hydrogen content of four different samples of the medium temperature region. The y-Axis shows the normalized total fluorescent yield which is the spectra for the bulk diamond. The peak at 285eV is related to the π^* of the $sp^2 + p$. The 289 eV peak is because of the σ^* bond of the sp hybridization.

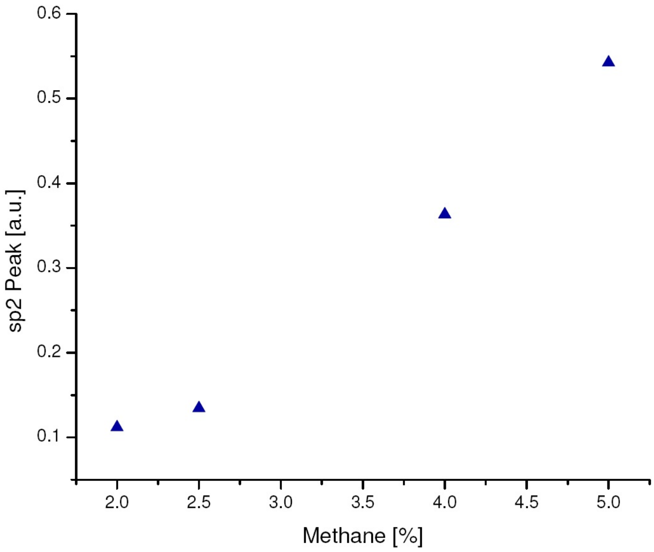

Figure 5.10: By estimating the peak height of the sp_2 out of figure 5.9 the graphite concentration was assumed. The graphite contents seems to be five times higher for the specimen with high Methane concentration

Figure 5.11 shows the raw Raman data. The diamond peak at 1332 cm^{-1} is clearly visible for most of the samples. Additionally the G-Band between 1435 and 1465 cm^{-1} is clearly visible. Some curves like #56 ($2.5\%CH_4, 840$ ℃) show a small hump around 1400 cm^{-1}. Some curves like #54 ($5\%CH_4, 830$ ℃) show a clear peak at 1150 cm^{-1} which is associated with the trans-polyacetylene mentioned above.

Good curve fits were obtained as shown in figure 5.12a and 5.12b but the D-band cannot be unique distinguished after the curve fitting. In some peaks a D-band could be estimated and in others it seemed to be too far away from the expected value around 1365 cm^{-1} [27]. The D'-mode band is missing within these curves, since it is barely visible in the raw data. Additional to the raw data shown in figure 5.11 which represents the center of the specimens measurements closer to the edge of the sample were conducted. Unfortunately it was impossible for me to obtain plausible and repeatable results with the used curve fitting software. Especially the results of the the same condor series one measured at the edge one in the center showed discrepancies. Data of #53 ($4\%CH_4, 850$ ℃) was missing and data of #54 ($5\%CH_4, 830$ ℃) was complicated to fit. No real quantitative analysis of the Methane series could be conducted.

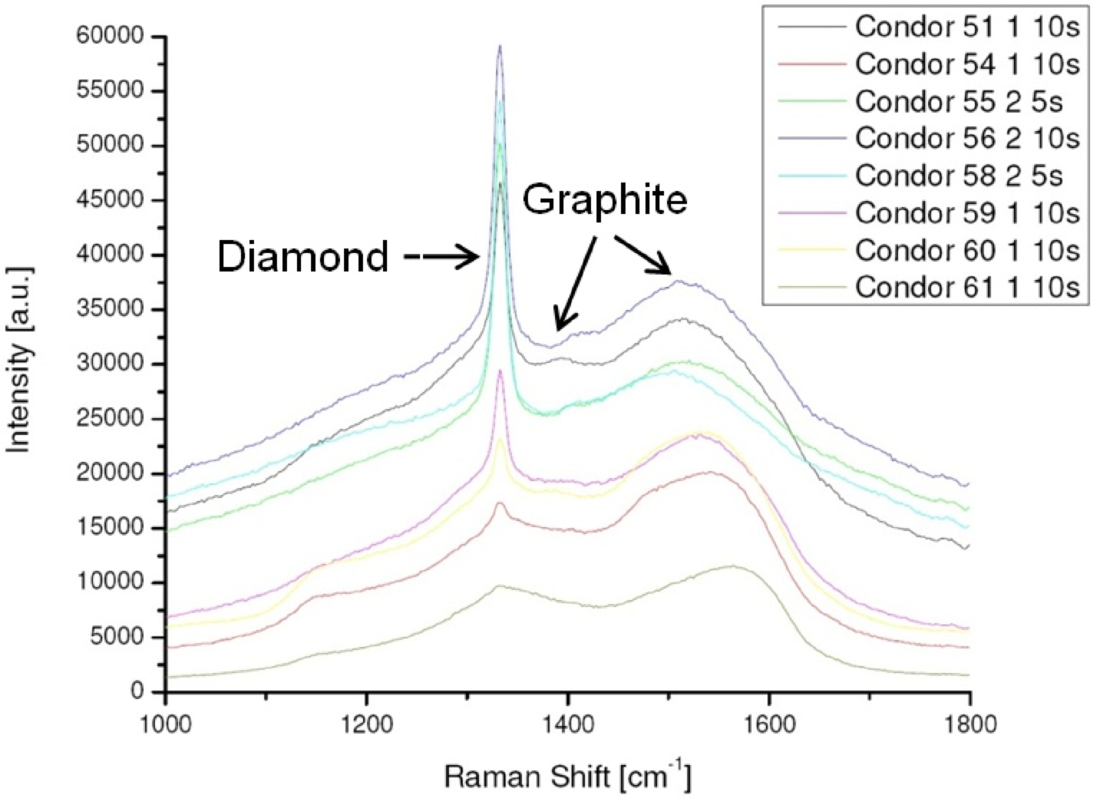

Figure 5.11: Raw data results of the Raman spectroscopy. It was assumed that the quality and the composition can be estimated out of the Raman spectra (page 23). But no proper curve fitting could be conducted and this assumption still has to be confirmed.

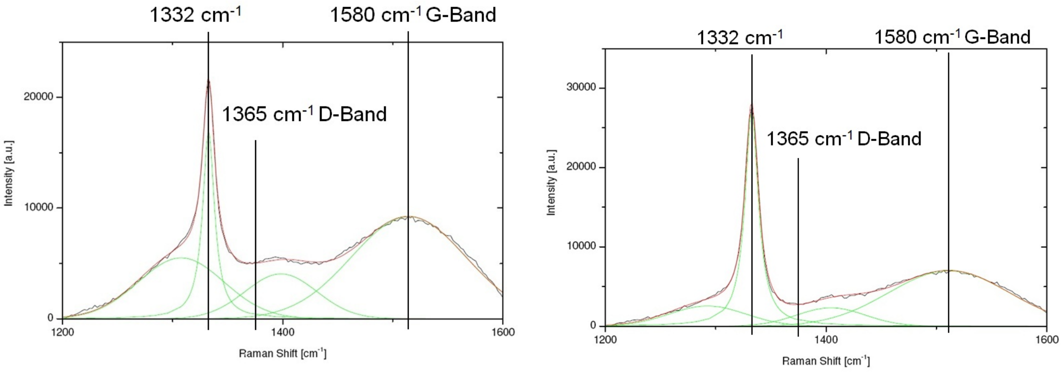

(a) #51

(b) #55

Figure 5.12: Both #55 ($2\%CH_4, 850$ °C) and #51 ($3\%CH_4, 830$ °C)confirm that the D-Band could not be fitted close to the expected frequency. All samples had a clear diamond peak even though the detection for graphite is several orders of magnitude more sensitive.

Figure 5.13 is the plot of the ERDA results. The abscissa named channel basically shows the depth of the measurement. Channel 300 is the surface of the sample which increases linear to Channel 0 a depth of about 0.5 μm. A SiO_2 measurement is used as reference. To get absolute Hydrogen values a simulation of one of the curves is necessary. In this case #61 ($5\%CH_4, 890$ °C) shows the highest yield and #55 ($2\%CH_4, 850$ °C) the lowest. The yield is directly related to the Hydrogen content of the samples. RUMP a special software for RBS and ERDA was used for the simulation. The result of the simulation is shown in figure 5.14 for #61 ($5\%CH_4, 890$ °C) which has 3,5 at. % of Hydrogen. The simulation of #55 ($2\%CH_4, 850$ °C) did not fit as well with the real values as #61 ($5\%CH_4, 890$ °C). To calculate the Hydrogen content for the other diamonds a linear Hydrogen distribution is assumed. Figure 5.13 shows a vertical red line at about channel 123. To minimize the influence of surface inhomogeneities, we analyzed the data around channel 127 which correspondents to a layer below the surface. The Hydrogen content of the examined diamond samples is shown in table 5.3.

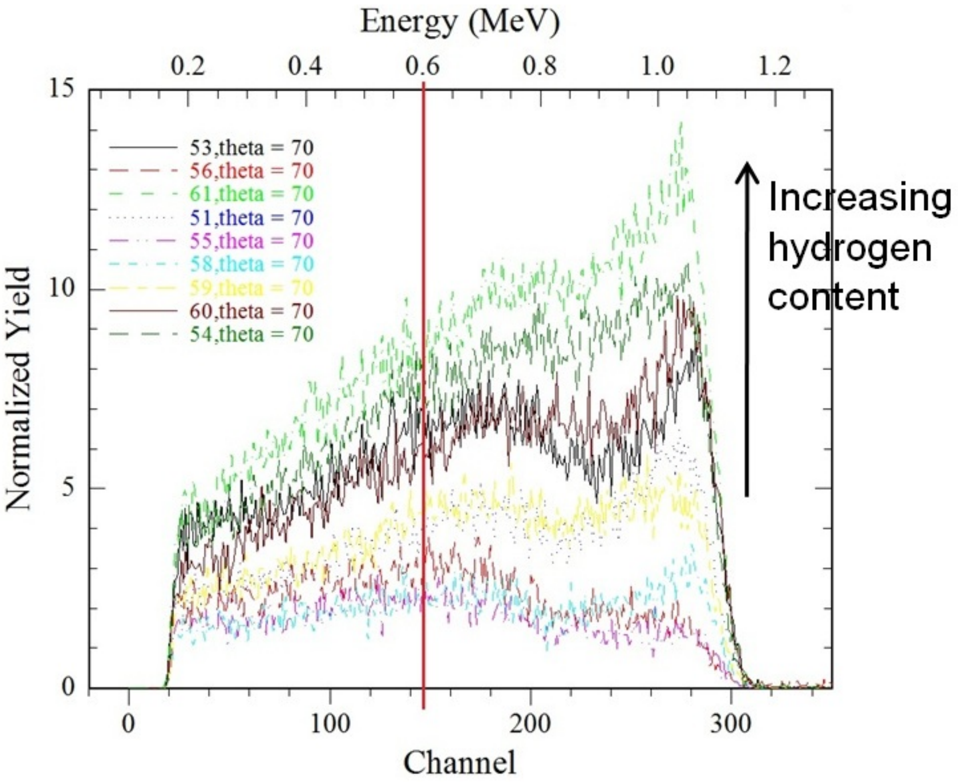

Figure 5.13: Shows the raw ERD data. Channel 300 is linked to the surface of the samples while channel 0 is about 0.5 μm in the sample. To avoid influenced of a dirty surface or being close to the noise level channel 170 was chosen for the analysis. A linear Hydrogen distribution was assumed which made it only necessary to simulate the Hydrogen content of one of the curves.

Table 5.3: Hydrogen concentration by ERDA and FTIR

Diamond	CH_4 [%]	Temperature [°C]	H_2[at. %] ERDA	H_2 [a.u.] FTIR
#51	3	830	1.6	2754
#53	4	850	2.4	3791.7
#54	5	830	3.2	4035.75
#55	2	850	0.9	916
#56	2.5	840	1.2	1381.9
#58	3	770	0.9	917
#59	3	890	1.8	2561.4
#60	4	850	2.7	4084
#61	5	∼890	3.5	3099.5

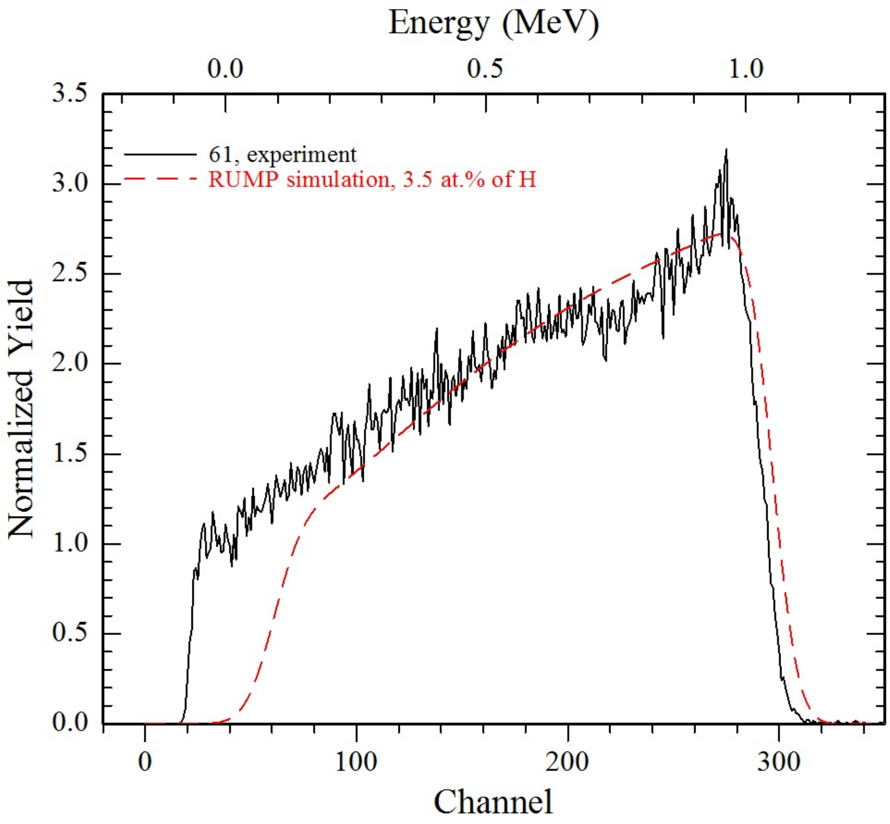

Figure 5.14: This reference spectra was simulated with RUMP. The raw data and the simulation almost match at channel 170

It is generally know that the Hydrogen concentration in diamond thin films increases with decreasing grain size [55]. Hydrogen is necessary in the feed gas because it etches graphite a few orders of magnitude faster than diamond, so that the introduction of atomic Hydrogen on the substrate surface greatly suppresses the co-deposition of graphite. Atomic Hydrogen also converts unsaturated carbon atoms to sp^3 by hydrogenation of sp and sp^2 carbon bonds [30]. Hydrogen was claimed to be found in grain boundaries [62, 57] and also be trapped at in-grain defects [41] . ERDA is not limited to measure just bonded Hydrogen in diamond but is also able to detect unbonded Hydrogen.

The Microscope, WLI, AFM and SEM results already showed that the higher the Methane concentration the smoother the surface. A smooth surface also indicates smaller grain sizes. The more smaller grains the higher the fraction of grain boundaries to bulk grains. Most of the Hydrogen is bounded within these boundaries which leads to higher Hydrogen concentrations in small grain sized materials. Figure 5.15 supports this theory since higher Methane concentrations lead to smaller grain sizes which increases the Hydrogen fraction in the diamond. These results are in good agreement with the results published by Sobia Allah Rakha et. al. in [55].

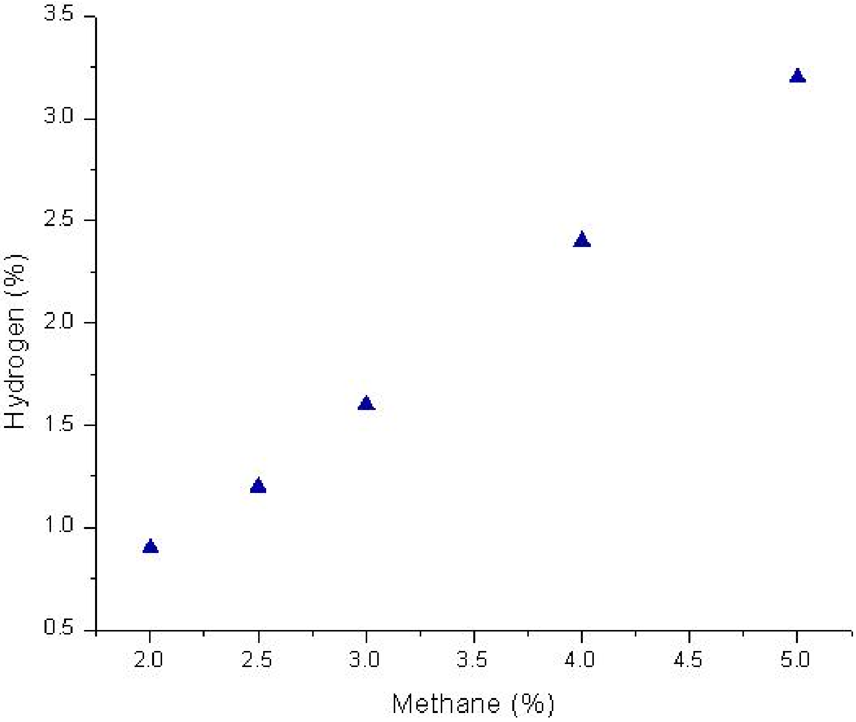

Figure 5.15: The Methane and Hydrogen dependency seems to be almost linear for the Methane series (all medium temperature, #51, #53-#56)

The FTIR results of the diamond films are shown in figure 5.16a and 5.16b. A polynomial baseline was subtracted from the raw data. Afterwards the data was fitted with six Gaussian functions. The peak fittings before and after this region were necessary to get better results with the used software. Depending on the curve fitting 2850 cm^{-1} and 2920 cm^{-1} are not always the dominant peaks in these curves. Unfortunately I was not able to improve the fitting results by fixing the parameters like suggested in [12]. Fixed parameters did not work properly with the software. Particularly the 2960 cm^{-1} and 3025 cm^{-1} peaks shifted often far from their actual positions. Proper peak assignment was especially hard for the peaks around 2820 cm^{-1} and 2832 cm^{-1} since these peaks are really close together. By C.J. Tang it was shown that the 2828 cm^{-1} peak visibility is dependent on the nucleation density and only shows up in poor quality CVD diamond [63, 64]. Since most of the curves had indication for one peak only in this region six Gaussian fits were used. Except one of the two #59 ($3\%CH_4, 890$ ℃) had two visible bands in this region and was fitted with 7 Gaussian functions then. Additionally the measuring resolution of the FTIR raw data was low which made the noisy data almost impossible to fit.

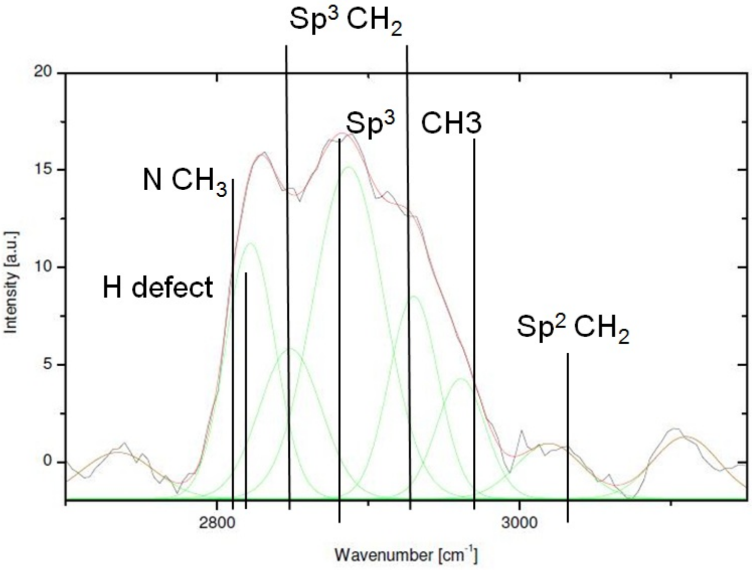

(a) #51

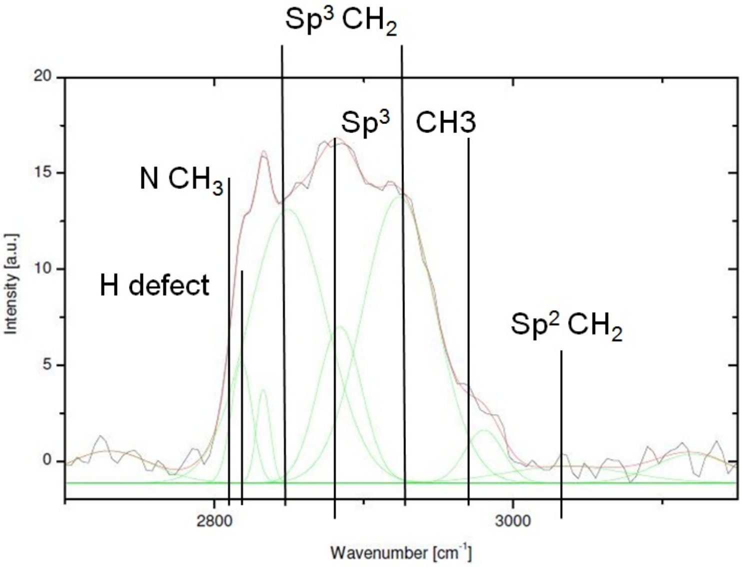

(b) #59

Figure 5.16: Figure 5.16a and 5.16b represent #51 ($3\% CH_4, 830$ and #59 ($3\% CH_4, 890$ ℃). Both graphs mainly show sp_3 related peaks which is everything below 3000 cm^{-1}. To estimate the Hydrogen content all the peak areas were added up. Thus different curve fitting like the sp^3CH_3 peak had no influence. To improve the results of the curve fitting two additional curves had to be fitted on the very left and right of the images.

To obtain the Hydrogen concentration in the samples the sum of the six or seven integrated peaks was calculated. Since there were two measurements of each of the Condor diamonds the average of the results was taken. Some of the samples showed a big deviation. Particularly #61 ($5\% CH_4, 890$ ℃, nanoseeding) had two different areas with 23% deviation. The reason for these big differences has to be further analyzed. In figure 5.17a and 5.17b the obtained Hydrogen results were plotted versus the Methane concentration of the diamonds. Since the thickness has an influence on the FTIR results (the thicker the more absorbtion) the lower graph shows the integrated area divided by the thickness. Both figures indicate a influence of the Methane on the Hydrogen. This basically confirms the ERDA results and S. Michaelson who proposes that smaller grains result in higher Hydrogen atom retention [44].

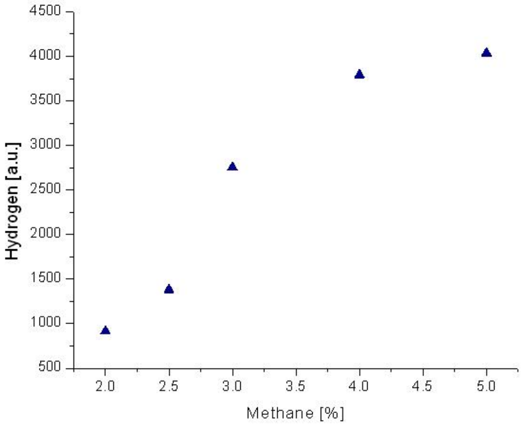

(a)

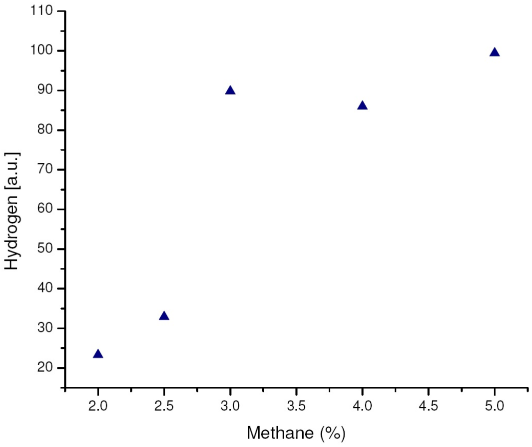

(b)

Figure 5.17: Both figures show the Hydrogen concentration estimated by FTIR and the Methane concentration. The allocations of them are very similar except that 5.17b seems to spread more. Since the FTIR measurement is dependent on the sample thickness the lower figure 5.17b should be more accurate. The FTIR area was divided by the sample thickness.

In Figure 5.18a and 5.18b the Hydrogen results from the FTIR and ERDA measurements are compared with each other. The FTIR characterization is in good agreement with the ERDA which is shown by the linear line in both graphs. The upper picture just shows one bigger deviation for the diamond with 3.5% Hydrogen according to ERDA which is #61 grown at high temperature, 5% Methane and nanoseeding. As already mentioned above the results of the two different FTIR measurements for #61 were very different. All diamonds except #61 show small deviations from a linear line. But if a steep slope is assumed in the beginning and it decreases between 2.5% and 3% CH_4 this would confirm the AFM results. The lower graph further highlights the deviations from the linear line for most of the samples. The #61 diamond is far off again. Additionally

#51 which had medium temperature and a medium Methane concentration (3%) shows a big deviation between both measurements. The reason for this discrepancy has to be further investigated to ensure that the correct correlations are found. It could be that the thickness was different at the measured sample due to a thicker thickness in the middle of the waver during the growth process or the ERDA measurement has to be repeated for this sample. The FTIR measurements did not show any deviations between the two obtained results. All in all it can be a promising approach that for further characterizations only FTIR measurements can be used for the Hydrogen concentration since ERDA is more complex. Table 5.2 summarizes these results.

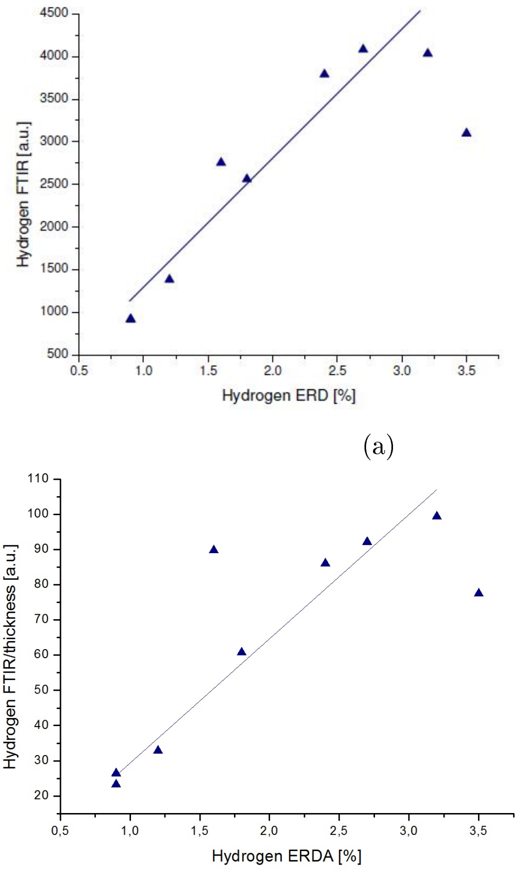

(a)

(b)

Figure 5.18: These graphs compare the ERDA and the FTIR Hydrogen analysis with each other. The linear line would proof equality of both measurements. In this case it seems that the upper figure 5.18a shows more linearity. The lower one 5.18b takes the sample thickness in consideration, which should normally lead to a better result. This deviation has to be further investigated.

Table 5.4: Density by Archimedes' principle

Diamond	Methane [%]	Temperature [°C]	Density [$\frac{g}{cm^3}$]
#51	3	830	3.48
#53	4	850	3.41
#54	5	830	3.35
#55	2	850	3.54
#56	2.5	840	3.54
#58	3	770	3.52
#59	3	890	3.46
#60	4	850	3.41
#61	5	~890	3.17

5.3 Mechanical properties

Mechanical properties were investigated with a density measurement and a three point bending test.

The density of the diamond films is shown in table 5.4. Again the same explanation can be used for these results. The increased amount of grain boundaries decreases the density. Natural diamond with a density of 3,52 $\frac{g}{cm^3}$ has large grains compared to these Nano-Crystalline samples. By calculating the density with the lattice constants and the atomic weight this density can be confirmed ($3.518\frac{g}{cm^3}$). Figure 5.19 confirms this behavior. With increasing Methane concentration, decreasing grain size the density decreases linear.

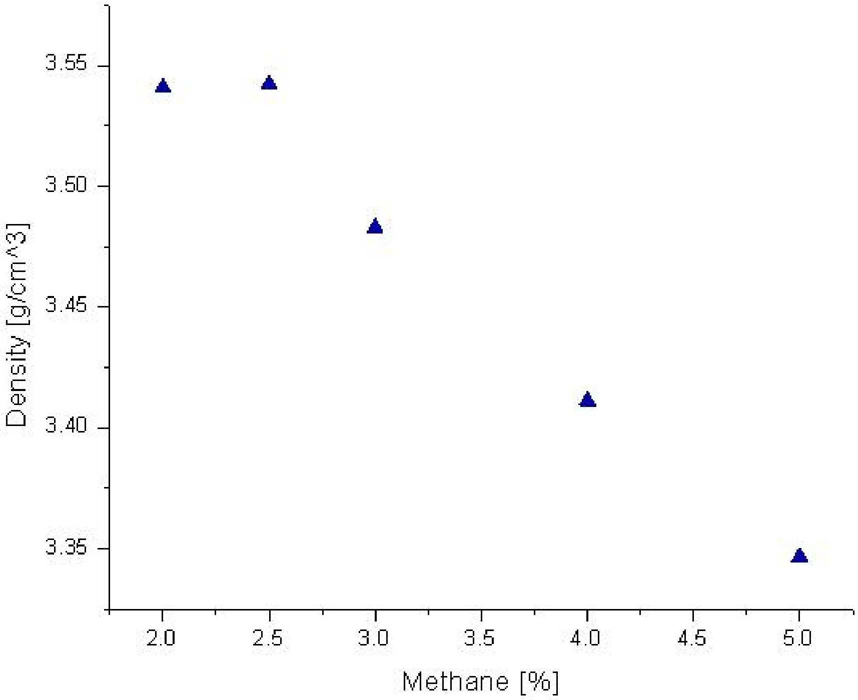

Figure 5.19: Diamonds of the medium temperature range (830-850℃) with different Methane concentrations (#51, #53-#56) are shown here vs the density. The density should be proportional to the grain size of the samples which is confirmed since the density decreases with higher Methane concentration.

The calculated Young's Modulus is shown in 5.20. Unfortunately these results do not show the expected values. Coarse grained samples were supposed to have a higher Young's Modulus than fine grained diamonds. #53 with 4% Methane shows higher values than #55 which only has 2% Methane. Additionally ballindenter and nanoindenter deviate from each other. To improve results the compliance of the insturment can be accounted for as done in [15].

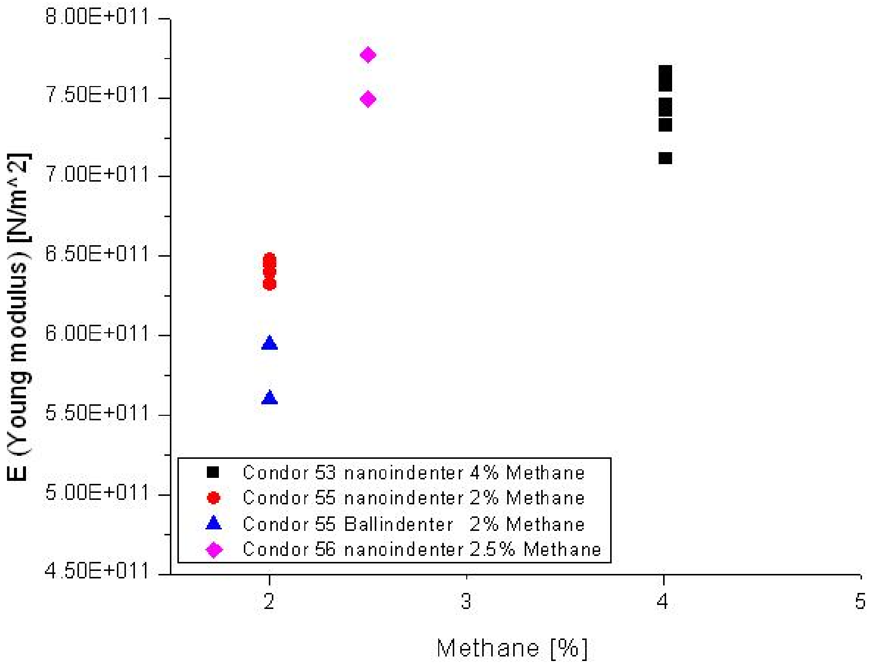

Figure 5.20: The Young's Modulus of three different medium temperature diamonds was calculated. Two different methods were used. The results are unexpected since it does not seem that there is any dependency at all

5.4 Grain Structure

Information from the grain structure can be obtained by the Raman spectroscopy and X-ray diffraction. Due to the unexpected Raman curves no characteristic figures were estimated, details on page 41 and 23.

In figure 5.21 the X-ray diffraction pattern of the diamonds is shown. Basically four major peaks are visible which represent the 111, 220 311 and 331 miller index lattice planes of diamonds. No other peaks were observed which confirms the purity of the diamond with no larger graphite precipitates. In this measurement the 220 peak has the highest intensity. For better comparison diamond powder and a theoretical diffractogram are shown. The diamond powder confirms the theoretical values which are just the bars, the higher the bar the higher the intensity. By comparing these values with the Nano-Crystalline Diamonds a difference is immediately visible. First the intensity of the 220 peak is higher than the 111 peak. This suggest a 110 fiber texture as discussed below. Second most of the sample peaks are broader than the reference. Third the 400 peak is not visible at all.

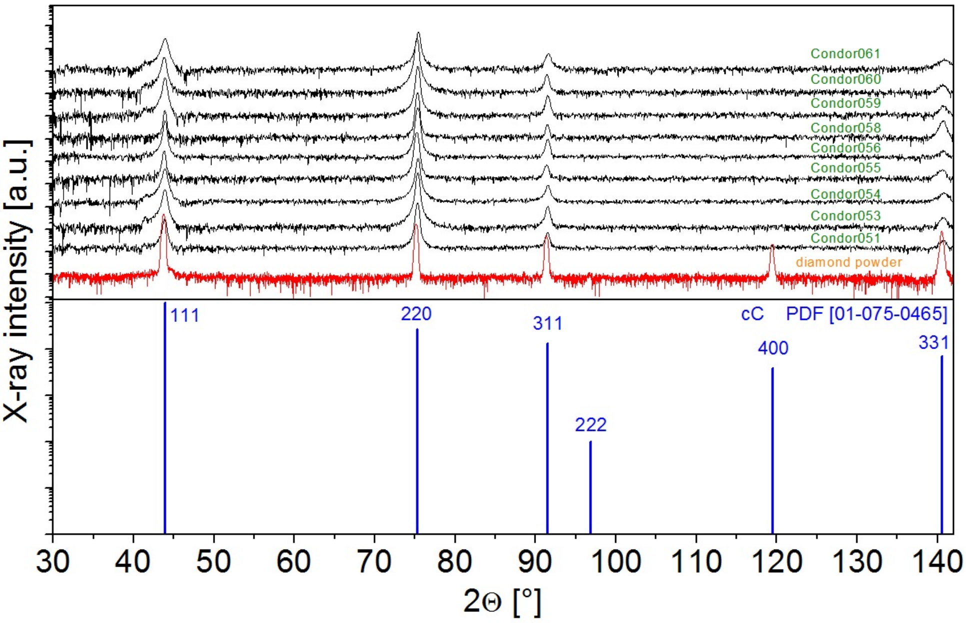

Figure 5.21: shows the x-ray diffraction results with two different references. The red line is pure diamond as well as the bars with the lattice planes (the higher the bar the higher the intensity). Comparing the diamond films with both references reveals many differences. The intensities are different, the peaks a broader and the 400 peak is missing. These are indicators for a texture.

Even though the measured patterns show some kind of unexpected values compared to the references the Scherrer equation was used to estimate the grain sizes. Figure 5.22 shows the results which are unexpected. All the calculated grain sizes are too small which means that our peaks are too broad and there is no big difference within the samples. The values estimated by the SEM cannot be confirmed. The results in figure 5.22 were obtained after a quantitative analysis with the MAUD program. Unfortunately the goniometer parameters were partly unknown and I need further understanding to properly use the program. In this case MAUD was used with 8 integrations and the default values to fit a reference curve on the measured values. Out of these fits the full with at half max was measured. The quality of the fits has to be improved that the above mentioned differences in the curves can be better covered.

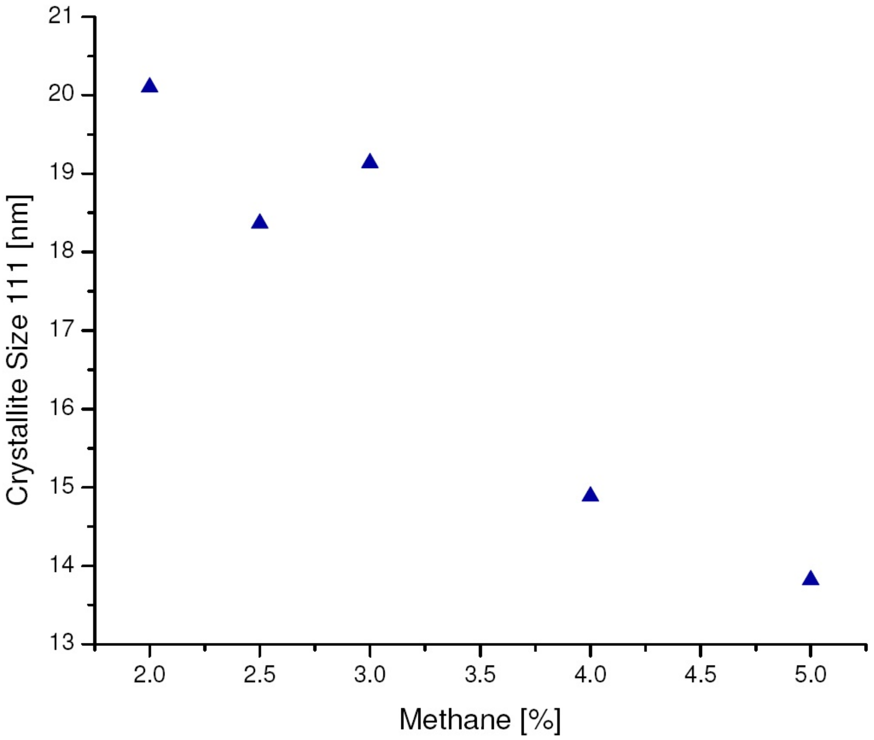

Figure 5.22: estimates the crystalline size vs. the Methane concentration for the diamonds of the medium temperature range (830-850℃) with different Methane concentrations (#51, #53-#56). Due to the texture these results show that the Scherrer equation cannot be used with textured samples. The results disagree with the SEM images.

Further investigation of the discrepancy of these peaks led to a texture analysis. This means the determination of preferred orientation of crystallites in polycrystalline material. This can explain why the 400 peak is missing, the width is unexpected and why the intensities of the peaks are different. A pole figure was measured of the #60 ($4\% CH_4, 850$ ℃, nanoseeding) sample which was grown on silicon and additionally of a diamond grown on a diamond single crystal substrate. Figure 5.23 shows the pole figure of the diamond grown on single crystal substrate. A 10 fold symmetry is visible represented by the 10 blue areas. The angle of 35° is associated with a 110 texture. Figure 5.24a represents one of the samples of this thesis. In this case the χ angle is plotted versus the intensity, the ϕ information is not visible here. Different than the diamond grown on the single crystal there is no in plane texture like the 10 fold symmetry visible here, but the texture at 35° (110) is still visible. Similar behavior is already observed for nanowires in [39, 75, 16]. Additional investigations are necessary to better understand the texture on these Nano-Crystalline Diamonds.

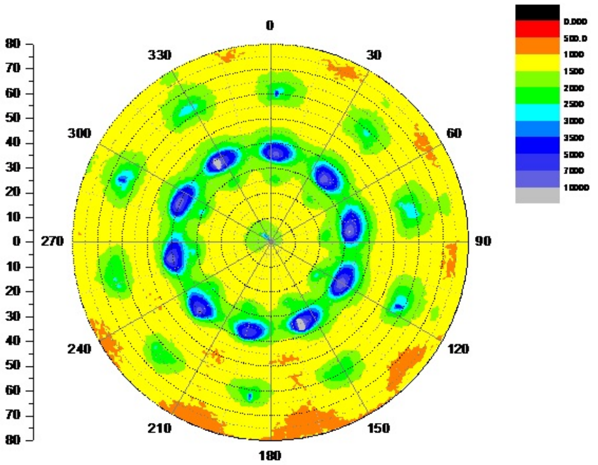

Figure 5.23: single crystal

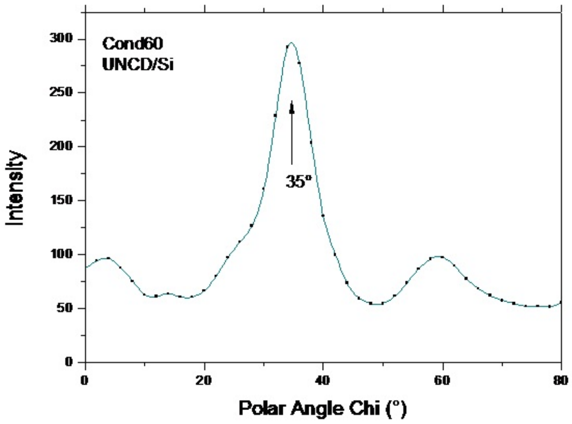

(a) #60 110 plane

Figure 5.24: 5.23 shows a 10 fold symmetry represented by the 10 blue areas. The angle of 35° is associated with a 110 texture (blue spots). Figure 5.24a represents #60 ($4\%CH_4, 850$ °C, nanoseeding). In this case the χ angle is plotted versus the intensity, the ϕ information is not visible here. Different than the diamond grown on the single crystal there is no in plane texture like the 10 fold symmetry visible here, but the texture at 35° (110) is still visible.

5.5 Further Dependencies

Almost all the characterization above were for the Methane series. The temperature series is similar to it which means the higher the deposition temperature, the smoother the surface. This is linked with a lower density, higher sp_2 concentration and higher Hydrogen content. The difference between the Methane series is that the high temperature diamond #59 ($3\%CH_4, 890$ ℃) was not as smooth as the higher Methane diamonds. It means that one cannot achieve smooth surfaces with just growing the diamonds at high temperatures and not changing any other parameters. The two nanoseeding samples further decreased the surface roughness as expected but on the other hand the Hydrogen and sp_2 content increased. Compared to the diamond #53 ($4\%CH_4, 850$ ℃) with the high Methane concentration of 4% (850°C) the differenece in roughness were very low, 11,5nm in the R_q value for the #60 ($4\%CH_4, 850$ ℃, nanoseeding, same parameters as #53 ($4\%CH_4, 850$ ℃) except nanoseeding).

Another way of connecting these results with easy measurements is shown in figure 5.25. As already mentioned above the roughness is related to the grain size which can be linked with Hydrogen and the graphite structures in the diamond. This indirectly means that one can estimate these values over the roughness. As example the Hydrogen content and the density are shown in this graph. The density almost perfect correlates with the roughness which means the smoother the surface the lower the density. Results for the Hydrogen concentration are similar but in this case the smoother the surface the higher the Hydrogen content.

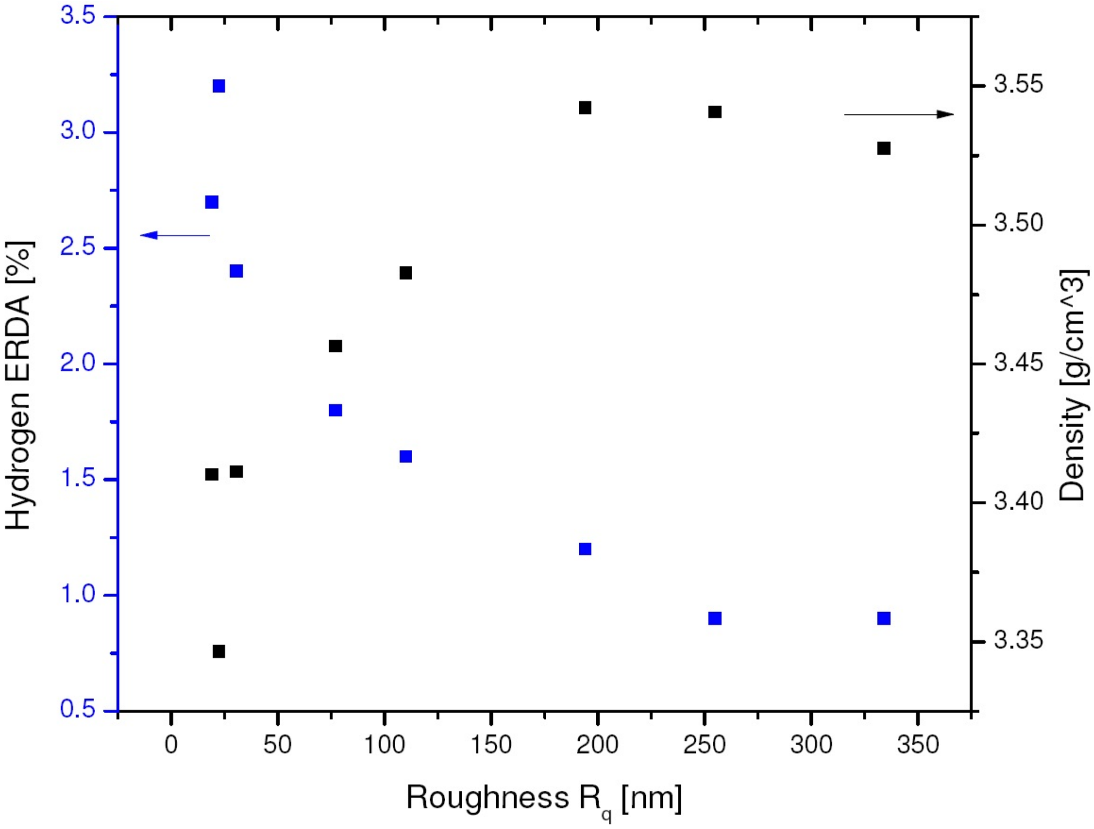

Figure 5.25: The roughness is most obviously linked with the grain size. By comparing the roughness with the ERDA and the density results it reveals that there is almost no change anymore after a roughness of 250nm R_q.

6 Conclusions and Outlook

In this thesis four major characteristics of diamonds were analyzed: the surface morphology, the grain structure, chemical composition and mechanical properties. All measurements were verified by another method to ensure the results. Nine different diamonds grown under different conditions were compared with each other and quantitative characterized. It was expected that higher Methane concentrations and higher temperature during the growth process influence the diamond to get smoother surfaces which are a requirement for inertial confinement fusion targets. On the other hand these two increased growth parameters lead to impurities in the diamond like Hydrogen, sp_2 hybridized carbon (graphite) and lower densities.

The surface morphology was determined by optical microscopy, scanning electron microscopy (SEM), atomic force microscopy and white light interferometry. The optical and measured results show that Methane and temperature influence the surface. A high Methane concentration has a bigger impact for obtaining a smooth surface than a higher temperature. The roughness can be further improved by using nanoseeding.

The grain structure was examined by x-ray diffraction, SEM and Raman spectroscopy. It was tried to get quality factors out of the Raman results which failed because of several uncertainties during the data analysis. Only a rough estimation of the grain size was done with the AFM and SEM images which still has to be verified by other methods. Transmission electron microscopy is planned for the future for accurate grain size estimation. X-ray diffraction did not work to get further grain size results due to a texture in the diamond. This texture will be additionally analyzed by electron backscatter diffraction a special method to detect preferred orientations of crystallites.

The chemical composition was identified with Elastic Recoil Detection, Fourier transform infrared- (FTIR), Raman spectroscopy and near edge x-ray absorption fine structure (NEXAFS). Estimating the hybridization of the carbon was done by NEXAFS. Unfortunately the quality of these results was not accurate enough to obtain quantitative values. The measurements will be repeated at the end of June 2010. Due to these results and Raman data at an uncommon frequency no estimation with the Raman data was possible. In theory one way to consider the quality of CVD diamond is the proportion of sp3-bonded carbon to sp2-bonded carbon in the sample. The Hydrogen concentration was examined with Elastic Recoil Detection and confirmed with FTIR. In future FTIR might be enough to estimate the Hydrogen content of similar samples. But still all these measurements confirmed the dependency that higher Methane content or higher temperature while growing increase the impurities.

J.G. Buijnsters reports to determine the Hydrogen concentration of amorphous carbon films by FTIR, ERDA, Raman and NEXAFS in [9]. The Condor diamonds are not amorphous but the results can be better linked with new NEXAFS results in future.

Maybe even the Raman spectroscopy can be used to get some Hydrogen data out of the plots. Further examination was with the current Raman and NEXAFS data not possible.

The mechanical properties were investigated with the Archimedes principle and a three point bending test. The test set up for the three point bending test has to be further improved due to some unexpected error during the measurements. Additionally it is planned for the future to examine the fracture toughness of the samples and to link these results with other characterizations. The Archimedes principle was used to obtain the density of the different diamonds. It must change with grain size and different composition of the samples. The density is an important factor for future fusion targets since the higher the density the more energy can be absorbed and the higher the fusion efficiency.

The current results with the above mentioned improvements are very promising that the grain size can be actually linked to the density, Hydrogen content, sp_2 concentration and mechanical properties. We plan to investigate pulsed deposited samples which are layers of microcrystalline and Nano-Crystalline Diamond. This composition might be a promising step for future diamond targets. These targets are supposed to have low impurities (Hydrogen and sp_2 carbon), a smooth surface and a high density.

7 Acknowledgement

I would like to thank my thesis advisor Jürgen Biener who supported my thesis at LLNL. Additionally I am glad for all the help from my colleagues at LLNL: Monika M Biener, Alex V. Hamza, Sergei Kucheyev, Lasse Landt, Edward Lindsey, Trevor M. Willey and Kuang Jen Wu.

Also I would like to thank Lutz Kirste, Christoph Wild, Eckhard Wörner and Marco Wolfer at Fraunhofer Institut fuer Festkörperphysik for manufacturing the diamonds as well as doing the Raman-, FTIR spectroscopy, WLI and XRD characterization.

Further I would like to thank Prof. Macian Juan for being my advisor at Technical University of Munich.

Bibliography

[1] Agilent Technologies. Scanning probe microscope (spm) acoustic ac. `http://www.home.agilent.com/agilent/editorial.jspx?cc=US&lc=eng&ckey=908266&id=908266`, 2010. [Website, taken on: 04/28/2010].

[2] Agilent Technologies. Scanning probe microscope (spm) contact modes. `http://www.home.agilent.com/agilent/editorial.jspx?cc=US&lc=eng&ckey=908261&id=908261`, 2010. [Website, taken on: 04/28/2010].

[3] J. Biener, D. D. Ho, C. Wild, E. Woerner, M. M. Biener, B. S. El-dasher, D. G. Hicks, J. H. Eggert, P. M. Celliers, G. W. Collins, N. E. Teslich, B. J. Kozioziemski, S. W. Haan, and A. V. Hamza. Diamond spheres for inertial confinement fusion. *Nuclear Fusion*, 49(11), 2009.

[4] J. Biener, P. B. Mirkarimi, J. W. Tringe, S. L. Baker, Y. Wang, S. O. Kucheyev, N. E. Teslich, K. J. J. Wu, A. V. Hamza, C. Wild, E. Woerner, P. Koidl, K. Bruehne, and H. J. Fecht. Diamond ablators for inertial confinement fusion. *Fusion Science and Technology*, 49(4):737–742, 2006.

[5] G. Binnig, C. F. Quate, and C. Gerber. Atomic force microscope. *Physical Review Letters*, 56(9):930–933, 1986.

[6] J. R. Bird and J. S. Williams. *Ion beams for materials analysis / edited by J.R. Bird and J.S. Williams.* Academic Press, Sydney :, 1989.

[7] R. T. Blunt. White light - a production worthy technique for measuring surface roughness on semiconductor wafers. *Proceedings of the International Conference on Compound Semiconductor Manufacturing Technology*, 2006.

[8] D. K. Bradley, J. H. Eggert, R. F. Smith, S. T. Prisbrey, D. G. Hicks, D. G. Braun, J. Biener, A. V. Hamza, R. E. Rudd, and G. W. Collins. Diamond at 800 gpa. *Physical Review Letters*, 102(7):075503 (4 pp.)–075503 (4 pp.), 2009.

[9] J. G. Buijnsters, R. Gago, I. Jimenez, M. Camero, F. Agullo-Rueda, and C. Gomez-Aleixandre. Hydrogen quantification in hydrogenated amorphous carbon films by infrared, raman, and x-ray absorption near edge spectroscopies. *Journal of Applied Physics*, 105(9):093510–093510–7, 2009.

[10] Terence J. Clark, Mark A. Banash, Richard W. Cruse, John Fech, Robert M. Mininni, and Stephen J. Rohman. The use of infrared interference spectra to measure ceramic coating thickness in a cvd reactor. *Thin Solid Films*, 254(1-2):7–9, 1995.

[11] P. Deák, J. Giber, and H. Oechsner. Mechanism of diamond growth in the presence of atomic hydrogen. *Surface Science*, 250(1-3):287 – 290, 1991.

[12] B. Dischler, C. Wild, W. Mullersebert, and P. Koidl. Hydrogen in polycrystalline diamond - an infrared-analysis. *Physica B*, 185(1-4):217–221, 1993.

[13] A. C. Ferrari and J. Robertson. Origin of the 1150-cm/sup -1/ raman mode in nanocrystalline diamond. *Physical Review B (Condensed Matter and Materials Physics)*, 63(12):121405/1–121405/4, 2001.

[14] J. Filik, P. W. May, S. R. J. Pearce, R. K. Wild, and K. R. Hallam. Xps and laser raman analysis of hydrogenated amorphous carbon films. *Diamond and Related Materials*, 12(3-7):974–978, 2003.

[15] M. Fátima Vales Silva, P. Hancock, and J. R. Nicholls. An improved three-point bending method by nanoindentation. *Surface and Coatings Technology*, 169-170:748–752, 2003.

[16] Xin Fu and et al. Re-entrant-groove-assisted vls growth of boron carbide five-fold twinned nanowires. *Chinese Physics Letters*, 26(8):086110, 2009.

[17] Polytec GmbH. Grundlagen der weißlicht-interferometrie. `http://www.polytec.com/ger/158_5797.asp`, 2010. [Website, taken on: 04/27/2010].

[18] Karl-Heinrich Grote and Jörg Feldhusen, editors. *DUBBEL – Taschenbuch für den Maschinenbau*. Springer, Berlin, 22. edition, 2007.

[19] S. W. Haan, D. A. Callahan, M. J. Edwards, B. A. Hammel, D. D. Ho, O. S. Jones, J. D. Lindl, B. J. MacGowan, M. M. Marinak, D. H. Munro, S. M. Pollaine, J. D. Salmonson, B. K. Spears, and L. J. Suter. Rev3 update of requirements for nif ignition targets. *Fusion Science and Technology*, 55(3):227–232, 2009.

[20] Alex Hamza. Cyrogenic targets for the national ignition campaign. NIC 2009 Seminar Series, 2009.

[21] Alex V. Hamza. Nscl annual report 2007. Status Report, 2007.

[22] M. S. Haque, H. A. Naseem, J. L. Shultz, W. D. Brown, S. Lal, and S. Gangopadhyay. Comparison of infrared, raman, photoluminescence, and x-ray photoelectron spectroscopy for characterizing arc-jet-deposited diamond films. *Journal of Applied Physics*, 83(8):4421–4429, 1998.

[23] MI Hoffert, K Caldeira, G Benford, DR Criswell, C Green, H Herzog, AK Jain, HS Kheshgi, KS Lackner, JS Lewis, HD Lightfoot, W Manheimer, JC Mankins, ME Mauel, LJ Perkins, ME Schlesinger, T Volk, and TML Wigley. Advanced technology paths to global climate stability: Energy for a greenhouse planet. *SCIENCE*, 298(5595):981–987, NOV 1 2002.

[24] Iter Organization. Pages - fusion fuels. `http://www.iter.org/sci/Pages/Default.aspx`, 2009. [website, taken on: 03/12/2010].

[25] M. J. Jackson, G. M. Robinson, H. Sein, W. Ahmed, N. Ali, and D. S. Misra. Surface characterization of (111) and (100) textured diamond coatings deposited to silicon. *Journal of Materials Engineering and Performance*, 14(5):666–670, 2005.

[26] T. Jawhari, A. Roid, and J. Casado. Raman spectroscopic characterization of some commercially available carbon black materials. *Carbon*, 33(11):1561–1565, 1995.

[27] Y. Kawashima and G. Katagiri. Fundamentals, overtones, and combinations in the raman-spectrum of graphite. *Physical Review B*, 52(14):10053–10059, 1995.

[28] MH Key. Fast track to fusion energy. *Nature*, 412(6849):775–776, Aug. 23 2001.

[29] D. S. Knight and W. B. White. Characterization of diamond films by raman-spectroscopy. *Journal of Materials Research*, 4(2):385–393, 1989.

[30] K. Kobashi, K. Nishimura, Y. Kawate, and T. Horiuchi. Synthesis of diamonds by use of microwave plasma chemical-vapor deposition - morphology and growth of diamond films. *Physical Review B*, 38(6):4067–4084, 1988.

[31] A. R. Krauss, O. Auciello, D. M. Gruen, A. Jayatissa, A. Sumant, J. Tucek, D. C. Mancini, N. Moldovan, A. Erdemir, D. Ersoy, M. N. Gardos, H. G. Busmann, E. M. Meyer, and M. Q. Ding. Ultrananocrystalline diamond thin films for mems and moving mechanical assembly devices. *Diamond and Related Materials*, 10(11):1952–1961, 2001.

[32] C. E. Kril and R. Birringer. Estimating grain-size distributions in nanocrystalline materials from x-ray diffraction profile analysis. *Philosophical Magazine A*, 77:621 – 640, 1998.

[33] S. O. Kucheyev, J. Biener, J. W. Tringe, Y. M. Wang, P. B. Mirkarimi, T. van Buuren, S. L. Baker, A. V. Hamza, K. Bruhne, and H. J. Fecht. Ultrathick, low-stress nanostructured diamond films. *Applied Physics Letters*, 86(22), 2005.

[34] S. Ravi Kumar, M.K. Panigrahi, S.K. Thakur, K.U. Kainer, M. Chakraborty, and B.K. Dhindaw. Characterization of stress in reinforcements in magnesium based squeeze infiltrated cast hybrid composites. *Materials Science and Engineering: A*, 415(1-2):207 – 212, 2006.

[35] Lawrence Livermore National Laboratory. Fusion science: Fast ignition, nif & photon s. `https://lasers.llnl.gov/science_technology/fusion_science/fast_ignition.php`, 2009. [Website, taken on: 11/19/2009].

[36] Pierre Lespade, André Marchand, Michel Couzi, and Francis Cruege. Caracterisation de materiaux carbones par microspectrometrie raman. *Carbon*, 22(4-5):375–385, 1984.

[37] J LINDL. Development of the indirect-drive approach to inertial confinement fusion and the target physics basis for ignition and gain. *Physics of Plasmas*, 2(11):3933–4024, Nov. 1995.

[38] JD Lindl, P Amendt, RL Berger, SG Glendinning, SH Glenzer, SW Haan, RL Kauffman, OL Landen, and LJ Suter. The physics basis for ignition using indirect-drive targets on the National Ignition Facility. *Physics of Plasmas*, 11(2):339–491, FEB 2004.

[39] Tao Ling, Huimin Yu, Xiaohua Liu, Zhongyao Shen, and Jing Zhu. Five-fold twinned nanorods of fcc fe: Synthesis and characterization. *Crystal Growth & Design*, 8(12):4340–4342, 2008.

[40] M. J. Lipp, V. G. Baonza, W. J. Evans, and H. E. Lorenzana. Nanocrystalline diamond: Effect of confinement, pressure, and heating on phonon modes. *Physical Review B*, 56(10):5978–5984, 1997.

[41] RD Maclear, JE Butler, SH Connell, BP Doyle, IZ Machi, DB Rebuli, JPF Sellschop, and E Sideras-Haddad. The distribution of hydrogen in polycrystalline CVD diamond. *Diamond and Related Materials*, 8(8-9):1615–1619, AUG 1999.

[42] R. L. McCrory, D. D. Meyerhofer, R. Betti, R. S. Craxton, J. A. Delettrez, D. H. Edgell, V. Y. Glebov, V. N. Goncharov, D. R. Harding, D. W. Jacobs-Perkins, J. P. Knauer, F. J. Marshall, P. W. McKenty, P. B. Radha, S. P. Regan, T. C. Sangster, W. Seka, R. W. Short, S. Skupsky, V. A. Smalyuk, J. M. Soures, C. Stoeckl, B. Yaakobi, D. Shvarts, J. A. Frenje, C. K. Li, R. D. Petrasso, and F. H. Seguin. Progress in direct-drive inertial confinement fusion. *Physics of Plasmas*, 15(5), 2008.

[43] K. M. McNamara, K. K. Gleason, and C. J. Robinson. Quantitative correlation of infrared-absorption with nuclear-magnetic-resonance measurements of hydrogen content in diamond films. *Journal of Vacuum Science & Technology a-Vacuum Surfaces and Films*, 10(5):3143–3148, 1992.

[44] Shaul Michaelson, Orna Ternyak, Rozalia Akhvlediani, and Alon Hoffman. The impact of diamond grain size on hydrogen concentration, bonding configuration, and electron emission properties of polycrystalline-diamond films. *Chemical Vapor Deposition*, 14(7-8):196–212, 2008.

[45] GH Miller, EI Moses, and CR Wuest. The National Ignition Facility. *Optical Engineering*, 43(12):2841–2853, DEC 2004.

[46] GH Miller, EI Moses, and CR Wuest. The National Ignition Facility: enabling fusion ignition for the 21st century. *Nuclear Fusion*, 44(12):S228–S238, Dec. 2004.

[47] E. I. Moses. Ignition on the national ignition facility: a path towards inertial fusion energy. *Nuclear Fusion*, 49(10), 2009.

[48] E. I. Moses, T. D. de la Rubia, E. Storm, J. F. Latkowski, J. C. Farmer, R. P. Abbott, K. J. Kramer, P. F. Peterson, H. F. Shaw, and R. F. Lehman. A sustainable nuclear fuel cycle based on laser inertial fusion energy. *Fusion Science and Technology*, 56(2):547–565, 2009.

[49] J Nuckolls, A Thiessen, L Wood, and Zimmerma.G. Laser Compression of Matter to super-high densities - thermonuclear (CTR) applications. *Nature*, 239(5368):139–&, 1972.

[50] JH Nuckolls. The Feasibility of inertial-confinement fusion. *Physics Today*, 35(9):24–31, 1982.

[51] S. P. Obenschain, J. D. Sethian, and A. J. Schmitt. A laser based fusion test facility. *Fusion Science and Technology*, 56(2):594–603, 2009.

[52] F. Peter. *Z Phys.* unknown, 1923. cross reference actual book was not available.

[53] R. Pfeiffer, H. Kuzmany, N. Salk, and B. Gunther. Evidence for trans-polyacetylene in nanocrystalline diamond films from h-d isotropic substitution experiments. *Applied Physics Letters*, 82(23):4149–4150, 2003.

[54] L. C. Qin, D. Zhou, A. R. Krauss, and D. M. Gruen. Tem characterization of nanodiamond thin films. *Nanostructured Materials*, 10(4):649–660, 1998.

[55] Sobia Allah Rakha, Cao Jianqing, Xia Huihao, Yu Guojun, Dezhang Zhu, and Jinlong Gong. Incorporation of hydrogen in diamond thin films. *Diamond and Related Materials*, 18(10):1247–1252, 2009.

[56] PH Rebut, A Gibson, M Huguet, JM Adams, B Alper, H Altmann, A Andersen, and et al. Fusion Energy-Production from a Deuterium-Tritium Plasma in the Jet Tokamak. *NUCLEAR FUSION*, 32(2):187–203, Feb. 1992.

[57] P Reichart, G Datzmann, A Hauptner, R Hertenberger, C Wild, and G Dollinger. Three-dimensional hydrogen microscopy in diamond. *SCIENCE*, 306(5701):1537–1540, NOV 26 2004.

[58] A. Sadezky, H. Muckenhuber, H. Grothe, R. Niessner, and U. Pöschl. Raman microspectroscopy of soot and related carbonaceous materials: Spectral analysis and structural information. *Carbon*, 43(8):1731–1742, 2005.

[59] S. R. Sails, D. J. Gardiner, M. Bowden, J. Savage, and D. Rodway. Monitoring the quality of diamond films using raman spectra excited at 514.5 nm and 633 nm. *Diamond and Related Materials*, 5(6-8):589–591, 1996.

[60] T. Sharda, T. Soga, and T. Jimbo. Optical properties of nanocrystalline diamond films by prism coupling technique. *Journal of Applied Physics*, 93(1):101–105, 2003.

[61] R. A. Sprague. Surface-roughness measurement using white-light speckle. *Applied Optics*, 11(12):2811, 1972.

[62] DF Talbot-Ponsonby, ME Newton, JM Baker, GA Scarsbrook, RS Sussmann, AJ Whitehead, and S Pfenninger. Multifrequency EPR, H-1 ENDOR, and saturation recovery of paramagnetic defects in diamond films grown by chemical vapor deposition. *Physical Review B*, 57(4):2264–2270, JAN 15 1998.

[63] C. J. Tang, A. J. Neves, and A. J. S. Fernandes. Influence of nucleation on hydrogen incorporation in cvd diamond films. *Diamond and Related Materials*, 11(3-6):527 – 531, 2002.

[64] C. J. Tang, A. J. Neves, L. Rino, and A. J. S. Fernandes. The 2828 cm-1 c-h related ir vibration in cvd diamond. *Diamond and Related Materials*, 13(4-8):958–964, 2004.

[65] E. Titus, D. S. Misra, A. K. Sikder, P. K. Tyagi, M. K. Singh, A. Misra, N. Ali, G. Cabral, V. F. Neto, and J. Gracio. Quantitative analysis of hydrogen in chemical vapor deposited diamond films. *Diamond and Related Materials*, 14(3-7):476–481, 2005.

[66] T. Ungar. Micro structural parameters from x-ray diffraction peak broadening. *Scripta Materialia*, 51(8):777–781, 2004.

[67] John C. Vickerman. *Surface Analysis - The Principal Techniques*. Wiley, July 1997.

[68] X. H. Wang, L. Pilione, W. Zhu, W. Yarbrough, W. Drawl, and R. Messier. Infrared optical-properties of cvd diamond films. *Journal of Materials Research*, 5(11):2345–2350, 1990.

[69] William M. Sharp. Heavy ion fusion tutorial. `http://hif.lbl.gov/tutorial/tutorial.html`, 2001. [website, taken on: 03/12/2010].

[70] A. Leigh Winfrey. Nanocrystalline diamond deposition for friction applications. Master's thesis, North Carolina State University, 2007.

[71] M. Wiora. High wear resistant and ultra-hard nanocrystalline diamond films. *Proceedings Of The ASME/STLE International Joint Tribology Conference*, 2009.

[72] M. Wiora. Ultra-hard and high wear resistant nanocrystalline diamond films. CMMD Seminar Series At Lawerence Livermore Nationa Laboratory, 2009.

[73] M. Wiora, K. Brühne, A. Flöter, P. Gluche, T. M. Willey, S. O. Kucheyev, A. W. Van Buuren, A. V. Hamza, J. Biener, and H. J. Fecht. Grain size dependent mechanical properties of nanocrystalline diamond films grown by hot-filament cvd. *Diamond and Related Materials*, 18(5-8):927–930, 2009.

[74] A. Wittstock, V. Zielasek, J. Biener, C. M. Friend, and M. Baumer. Nanoporous Gold Catalysts for Selective Gas-Phase Oxidative Coupling of Methanol at Low Temperature. *Science*, 327(5963):319–322, 2010.

[75] Bin Wu, Andreas Heidelberg, John J. Boland, John E. Sader, Sun, and Li. Microstructure-hardened silver nanowires. *Nano Letters*, 6(3):468–472, 2006.

[76] J. C. Wyant. White light interferometry. *Proceedings of SPIE*, 4737:98–107, 2002.

[77] Z. Zhang, F. Zhou, and E. J. Lavernia. On the analysis of grain size in bulk nanocrystalline materials via x-ray diffraction. *Metallurgical and Materials Transactions a-Physical Metallurgy and Materials Science*, 34A(6):1349–1355, 2003.

[78] Richard Zsigmondy. *Kolloidchemie : Ein Lehrbuch / von Richard Zsigmondy*. Leipzig : Spamer, 1920. Beigefügtes Werk Mit e. Beitrag: Bestimmung d. inneren Struktur u. d. Grösse von Kolloidteilchen mittels Röntgenstrahlen / von P. Scherrer.

List of Figures